Electro-optical properties of semiconductor quantum dots: Application to quantum information processing

Electro-optical properties of semiconductor quantum dots: Application to quantum information processing

Eliana Biolatti,[1,2] Irene D'Amico,[1,3] Paolo Zanardi,[1,3] and Fausto Rossi[1,2,3]
[1]*Istituto Nazionale per la Fisica della Materia (INFM), Corso Perrone 24, 16152 Genova, Italy*
[2]*Dipartimento di Fisica, Politecnico di Torino, Corso Duca degli Abruzzi 24 I-10129 Torino, Italy*
[3]*Institute for Scientific Interchange (ISI), Villa Gualino, Viale Settimio, Severo 65, I-10133 Torino, Italy*
(Received 17 August 2001; published 18 January 2002)

A detailed analysis of the electro-optical response of single as well as coupled semiconductor quantum dots is presented. This is based on a realistic—i.e., fully tridimensional—description of Coulomb-correlated few-electron states, obtained via a direct-diagonalization approach. More specifically, we investigate the combined effect of static electric fields and ultrafast sequences of multicolor laser pulses in the few-carrier, i.e., low-excitation regime. In particular, we show how the presence of a properly tailored static field may give rise to significant electron-hole charge separation; these field-induced dipoles, in turn, may introduce relevant exciton-exciton couplings, which are found to induce significant—both intradot and interdot—biexcitonic splittings. We finally show that such few-exciton systems constitute an ideal semiconductor-based hardware for an *all optical* implementation of quantum information processing.

DOI: 10.1103/PhysRevB.65.075306 PACS number(s): 03.67.Lx, 71.35.Cc, 73.21.La

I. INTRODUCTION

In the past years increasing interest has been focused on semiconductor nanostructures.[1] This is mainly due to their low-dimensional character, which allows one to tailor carrier quantum confinement as well as Coulomb interaction. As a result, this has allowed one to fabricate nanostructured systems with a properly designed density-of-states which, in turn, exhibit an increased optical efficiency as well as a reduction of energy-relaxation and dephasing processes.[2] For the case of two- and one-dimensional nanostructures, i.e., quantum wells and wires, however, we deal with a partial carrier confinement, i.e., the single-particle energy spectrum is still continuous. This allows one to describe their many-body ultrafast optical response in terms of the usual mean-field approaches, typical of bulk systems.[3]

The real scientific and technological ''revolution'' in the field was the introduction of quasi-zero-dimensional (0D) systems, called semiconductor quantum dots.[4] Compared to systems of higher dimensionality—such as quantum wells and wires—they have a discrete, i.e., atomiclike, energy spectrum and, more important, they exhibit genuine few-carrier effects. Generally speaking, going from quantum wells and wires to quantum dots (QD's) we move from many-electron systems to few-electron ones. This implies a radical change in the theoretical schemes[5] as well as in the experimental techniques[6] used to study such quasi-0D nanostructures, often referred to as *semiconductor macroatoms*. Apart from their relevance in terms of basic physics, these novel semiconductor nanostructures have attracted general attention because of their technological applications: these range from laser emitters[7] to charge-storage devices,[8] from fluorescent biological markers[9] to quantum information processing devices.[10]

In QD's, the flexibility typical of semiconductors in controlling carrier densities has been brought to its extreme: it is possible to electrically inject single electrons[11] or to photogenerate in a QD a single Coulomb-correlated electron-hole pair, i.e., a single exciton.[12,13] It is even possible to detect the single-exciton decaying energy emission.[12,13] The quantized, atomiclike, energy structure of QD's allows for a rich optical spectrum and for a weak interaction of the QD system with environmental degrees of freedom (such as phonons, plasmons, etc.). This latter feature implies that the quantum evolution of the carrier subsystem is affected by low decoherence.[14]

Moreover, their reduced spatial extension—up to few nanometers—leads to an increase of two-body interactions among carriers and to stronger Coulomb-correlation effects.[5] The latter may be used to design a variety of *single-electron devices*. In particular, as we shall show, they can be employed to design *fully optical quantum gates*, as recently proposed in Ref. 15. Indeed, the continuous progress in QD fabrication and characterization[16] let us foresee a near future in which it will be possible to exactly tailor the few-carrier and optical properties of these 0D systems. In this respect, a step forward has been recently made by the analysis and understanding of a single-QD excitonic emission spectrum,[13,17] that uncovered ''hidden'' symmetries in isolated QD structures, analogous to Hund's rules[13] for real atoms. These symmetries imply that, under suitable conditions, Coulomb correlations among excitons in the same dot cancel.

The primary goal of this paper is twofold. On the one hand, we shall present a detailed investigation of the electro-optical response of single as well as coupled QD structures. More specifically, we shall focus on the combined effect of static electric fields and ultrafast multicolor laser pulses. Our investigation will present a variety of field-induced effects unexplored so far; in particular, we shall show how a properly tailored external field can be used to induce or reinforce exciton-exciton Coulomb coupling both in single and coupled QD structures. On the other hand, we shall discuss the application of such field-induced few-exciton effects to

design a *semiconductor-based fully optical quantum information processing strategy*.[15]

The paper is organized as follows. In Sec. II we shall introduce our theoretical approach for the analysis of the electro-optical response of QD structures. Section III presents a detailed investigation of the excitonic as well as biexcitonic response of prototypical semiconductor macroatoms and molecules in the presence of an applied static field. In Sec. IV our quantum information processing strategy is discussed and a few simulated experiments of basic quantum information/computation (QIC) operations are presented. Finally, in Sec. V we shall summarize and draw some conclusions.

II. THEORETICAL APPROACH

The physical system under investigation is a gas of electron-hole pairs confined in a quasi-0D semiconductor structure, i.e., a single as well as a multiple QD. In this case, the total Hamiltonian of our semiconductor nanostructure can be regarded as the sum of two terms, $\mathbf{H}=\mathbf{H}^{\circ}+\mathbf{H}'$: A term $\mathbf{H}^{\circ}$ describing the correlated electron-hole subsystem, i.e., free carriers plus confinement potential plus carrier-carrier Coulomb interaction, and a term $\mathbf{H}'$ describing the interaction of the carrier subsystem with coherent-light sources and environmental degrees of freedom, i.e., carrier-light plus carrier-phonon interactions.

A. Single-particle description

Let us first consider the gas of noninteracting carriers, electrons (e) and holes (h) confined within the quasi-0D semiconductor structure. The quantum confinement can be described in terms of an effective potential $V_c^{e/h}$ whose height is dictated by the conduction/valence band discontinuities. Since the energy region of interest is relatively close to the band gap ϵ_{gap} of the semiconductors forming our heterostructure, we shall describe the bulk band structure in terms of the usual effective-mass approximation.[18] In addition, since the confinement potential $V_c^{e/h}$ is a slowly varying function on the scale of the lattice periodicity, we shall work within the ''envelope-function'' picture.[19]

Within such approximation scheme, the noninteracting carriers in our quasi-0D structure are then described by the following Schrödinger equation:

$$\left[-\frac{\hbar^2\nabla_{\mathbf{r}}^2}{2m_{e/h}}+V_c^{e/h}(\mathbf{r})\right]\psi_{i/j}(\mathbf{r})=\epsilon_{i/j}\psi_{i/j}(\mathbf{r}), \tag{1}$$

where $m_{e/h}$ is the bulk effective mass for electrons/holes while i/j denotes the set of single-particle quantum numbers, including charge as well as spin degrees of freedom.[20] Here, $\psi_{i/j}(\mathbf{r})$ is the envelope function of state $i(j)$, the eigenvalues $\epsilon_{i/j}$ correspond to the energy levels of the carriers induced by the confinement-potential profile $V_c^{e/h}$; since the latter—for any realistic semiconductor nanostructure—is finite, the lowest part of the single-particle energy spectrum $\epsilon_{i/j}$ is discrete, while for increasing energies it evolves into a continuum. The different approaches commonly employed for the solution of Eq. (1) are described in Appendix A; according to the energy region of interest, they range from direct three-dimensional (3D) plane-wave expansions, to factorized-state solutions, or to simplified two-dimensional parabolic-potential models.

B. Coulomb-correlated carrier system

Given the above single-particle representation $\{i\}(\{j\})$ for electrons (holes)—i.e., the set of 3D eigenfunctions $\psi_i(\mathbf{r})\equiv\langle\mathbf{r}|i\rangle$ $[\psi_j(\mathbf{r})\equiv\langle\mathbf{r}|j\rangle]$ and the corresponding energy levels $\epsilon_i(\epsilon_j)$—let us now introduce the following creation and destruction operators for electrons and holes

$$|i\rangle c_i^{\dagger}|0\rangle\rightarrow|0\rangle=c_i|i\rangle,\quad |j\rangle=d_j^{\dagger}|0\rangle\rightarrow|0\rangle=d_j|j\rangle, \tag{2}$$

where $|0\rangle$ denotes the electron-hole vacuum state. Within such second-quantization picture, the single-particle Hamiltonian, i.e., the Hamiltonian describing the noninteracting carriers within our 0D confinement potential, can be written as

$$\mathbf{H}^c=\mathbf{H}^e+\mathbf{H}^h=\sum_i \epsilon_i c_i^{\dagger}c_i+\sum_j \epsilon_j d_j^{\dagger}d_j. \tag{3}$$

The carriers (electrons and holes) within our quasi-0D nanostructure, however, interact via the two-body Coulomb potential $V(\mathbf{r}-\mathbf{r}')$. Due to such interaction, several correlation effects take place. Here, only processes conserving the total number of carriers are considered, thus Auger recombination and impact ionization are neglected. Such processes are known to become important only at very high densities and at energies high up in the band.[21] In this case the Hamiltonian describing carrier-carrier interaction within our single-particle i/j picture can be written as

$$\begin{aligned}\mathbf{H}^{cc}&=\mathbf{H}^{ee}+\mathbf{H}^{hh}+\mathbf{H}^{eh}\\&=\frac{1}{2}\sum_{i_1,i_2,i_3,i_4}V_{i_1i_2i_3i_4}c_{i_1}^{\dagger}c_{i_2}^{\dagger}c_{i_3}c_{i_4}\\&\quad+\frac{1}{2}\sum_{j_1,j_2,j_3,j_4}V_{j_1j_2j_3j_4}d_{j_1}^{\dagger}d_{j_2}^{\dagger}d_{j_s}d_{j_4}\\&\quad-\sum_{i_1,i_2,j_1,j_2}V_{i_1j_1j_2i_2}c_{i_1}^{\dagger}d_{j_1}^{\dagger}d_{j_2}c_{i_2},\end{aligned} \tag{4}$$

where

$$V_{l_1'l_2'l_2l_1}=\int d\mathbf{r}\int d\mathbf{r}'\,\psi_{l_1'}^{*}(\mathbf{r})\psi_{l_2'}^{*}(\mathbf{r}')V(\mathbf{r}-\mathbf{r}')\psi_{l_2}(\mathbf{r}')\psi_{l_1}(\mathbf{r}), \tag{5}$$

are the matrix elements of the Coulomb potential for the generic two-particle transition $l_1l_2\rightarrow l_1'l_2'$. The first two terms on the rhs of Eq. (4) describe the repulsive electron-electron and hole-hole interactions while the third one describes the attractive interaction between electrons and holes.

We stress the full 3D nature of the present approach based on the detailed knowledge of the 3D carrier wave function ψ. The explicit evaluation of the above matrix elements for a

generic 3D confinement-potential profile $V_c^{e/h}$, i.e., for a generic set of envelope functions $\psi_{i/j}$, is described in Appendix B.

Combining the single-particle Hamiltonian in Eq. (3) with the Coulomb-interaction term in Eq. (4), we get the following many-body Schrödinger equation for our Coulomb-correlated system:

$$\mathbf{H}^{\circ}|\Psi\rangle=(\mathbf{H}^{c}+\mathbf{H}^{cc})|\Psi\rangle=\mathcal{E}|\Psi\rangle. \tag{6}$$

Here, $|\Psi\rangle$ denotes the interacting many-body state in our Fock space and $\mathcal{E}$ the corresponding total energy.

Let us now introduce the total-number operators for electrons and holes

$$\mathbf{N}_e=\sum_i c_i^{\dagger}c_i, \quad \mathbf{N}_h=\sum_j d_j^{\dagger}d_j. \tag{7}$$

It is easy to show that the above global operators commute with the carrier Hamiltonian $\mathbf{H}^{\circ}$ in Eq. (6). We can therefore look for many-body states $|\Psi\rangle$ corresponding to a given number of electrons (N_e) and holes (N_h). In particular, we shall consider the case of intrinsic semiconductor materials,[18] for which $N_e=N_h$; in this case the good quantum number is the total number of electron-hole pairs: $N=N_e=N_h$ and the Schrödinger equation (6) can be rewritten as

$$\mathbf{H}^{\circ}|\lambda_N\rangle=\mathcal{E}_{\lambda_N}|\lambda_N\rangle, \tag{8}$$

where $|\lambda_N\rangle$ and $\mathcal{E}_{\lambda_N}$ denote, respectively, the λth many-body state and energy level corresponding to N electron-hole pairs.

For any given number N of electron-hole pairs we thus identify a subspace of the original Fock space, for which there exists a natural basis $\{|l_N\rangle\}$, given by the eigenstates of the single-particle Hamiltonian in Eq. (3):

$$\mathbf{H}^{c}|l_N\rangle=\epsilon_{l_N}|l_N\rangle. \tag{9}$$

Here, $l_N\equiv i_1,i_2,\ldots,i_N;\, j_1,j_2,\ldots,j_N$ is a compact notation for the set of noninteracting electron and hole single-particle quantum numbers corresponding to our N electron-hole pairs. Indeed, we have

$$|l_N\rangle\equiv|\{i_n j_n\}\rangle=\prod_{n=1}^{N} c_{i_n}^{\dagger}d_{j_n}^{\dagger}|0\rangle \tag{10}$$

and $\epsilon_{l_N}=\Sigma_{n=1}^{N}(\epsilon_{i_n}+\epsilon_{j_n})$.

The noninteracting basis set in Eq. (10) constitutes the starting point of the direct-diagonalization approach used for the solution of the many-body Schrödinger equation (8). Indeed, we can expand the unknown many-body state $|\lambda_N\rangle$ over our single-particle basis

$$|\lambda_N\rangle=\sum_{l_N} U_{l_N}^{\lambda_N}|l_N\rangle. \tag{11}$$

By inserting the above expansion into Eq. (8), the latter is transformed into the following eigenvalue problem:

$$\sum_{l_N'}(H^{\circ}_{l_N l_N'}-\mathcal{E}_{\lambda_N}\delta_{l_N l_N'})U_{l_N'}^{\lambda_N}=0, \tag{12}$$

where

$$H^{\circ}_{l_N l_N'}=\langle l_N|\mathbf{H}^{\circ}|l_N'\rangle=\epsilon_{l_N}\delta_{l_N l_N'}+\nu_{l_N l_N'} \tag{13}$$

are the matrix elements of the carrier Hamiltonian $\mathbf{H}^{\circ}$ in our single-particle basis. They are given by a diagonal—i.e., noninteracting—contribution plus a nondiagonal term given by the matrix elements of the Coulomb-interaction Hamiltonian in Eq. (4): $\mathcal{V}_{l_N l_N'}=\langle l_N|\mathbf{H}_{cc}|l_N'\rangle$. Their explicit form—which involves the various two-body Coulomb matrix elements in Eq. (5)—is given in Appendix C for the excitonic ($N=1$) and biexcitonic ($N=2$) case.

In the presence of Coulomb interaction, the Hamiltonian matrix in Eq. (13) is nondiagonal; therefore, the interacting many-body states $|\lambda_N\rangle$ are, in general, a linear superposition of all the single-particle states $|l_N\rangle$ [see Eq. (11)], whose coefficients $U_{l_N}^{\lambda_N}$ can be regarded as elements of the unitary transformation connecting the single-particle to the interacting basis $U_{l_N}^{\lambda_N}=\langle l_N|\lambda_N\rangle$.

The numerical evaluation of our Coulomb-correlated states is thus performed by direct diagonalization of the Hamiltonian matrix H° in Eq. (13), using a large—but finite—single-particle basis set.

C. Interaction with coherent light sources

The Coulomb-correlated carrier system described so far will interact strongly with electromagnetic fields in the optical range. For the case of a coherent light source—the one considered in this paper—the light-matter interaction Hamiltonian in our second-quantization picture can be written as.

$$\mathbf{H}'=-E(t)\sum_{ij}[\sigma_{ij}^{*}c_i^{\dagger}d_j^{\dagger}+\mu_{ij}d_j c_i], \tag{14}$$

where $E(t)$ is the classical light field and

$$\mu_{ij}=\mu_{\text{bulk}}\int \psi_i(\mathbf{r})\psi_j(\mathbf{r})d\mathbf{r} \tag{15}$$

is the dipole matrix element for the ij transition, μ_{bulk} being its bulk value. In the presence of a time-dependent coherent optical excitation the quantum-mechanical evolution of our electron-hole system will be described by the following time-dependent Schrödinger equation:

$$i\hbar\frac{d}{dt}|\Psi(t)\rangle=\mathbf{H}|\Psi(t)\rangle=(\mathbf{H}^{\circ}+\mathbf{H}')|\Psi(t)\rangle. \tag{16}$$

Contrary to the carrier Hamiltonian $\mathbf{H}^{\circ}$, the carrier-light term $\mathbf{H}'$ does not commute with the global number operators in Eq. (7). Indeed, the two terms in Eq. (14) describe, respectively, the light-induced creation and destruction of an electron-hole pair. Therefore, N is no more a good quantum number and the many-body state at time t is, in general, a linear superposition of all the correlated N-pair basis states

$$|\Psi(t)\rangle = \sum_N \sum_{\lambda_N} a_{\lambda_N}(t)|\lambda_N\rangle. \quad (17)$$

By inserting the above expansion into the time-dependent Schrödinger equation (16) we get

$$i\hbar \frac{d}{dt} a_{\lambda_N}(t) = \mathcal{E}_{\lambda_N} a_{\lambda_N}(t) + \sum_{N'} \sum_{\lambda'_{N'}} H'_{\lambda_N \lambda'_{N'}} a_{\lambda'_{N'}}(t), \quad (18)$$

where

$$H'_{\lambda_N \lambda'_{N'}} = \langle \lambda_N | \mathbf{H}' | \lambda'_{N'} \rangle \quad (19)$$

are the matrix elements of the light-matter Hamiltonian (14) within our interacting N-pair basis $\{\lambda_N\}$.

It can be easily shown (see Appendix C) that the above matrix elements are different from zero only for $N' = N \pm 1$; this confirms that the only possible transitions are $N \rightarrow N+1$ or $N+1 \rightarrow N$ which correspond, respectively, to the generation and destruction of Coulomb-correlated electron-hole pairs, i.e., excitons, discussed above. Moreover, we deal with well precise spin selection rules: the only matrix elements in Eq. (19) different from zero are those conserving the total spin of the carrier-light system. Indeed, the possible final states $|\lambda_N\rangle$ depend on the spin configuration of the initial many-body state $|\lambda'_{N'}\rangle$ as well as on the polarization of the electromagnetic field $E(t)$. In particular, we are allowed to create two excitons with opposite spin orientation (i.e., antiparallel-spin configuration) in the same orbital quantum state. In contrast, due to the Pauli exclusion principle, two excitons with the same spin orientation (i.e., parallel-spin configuration) cannot occupy the same orbital state.

By treating Eq. (18) within the standard time-dependent perturbation-theory approach and assuming a monochromatic light source of frequency ω, we can define the absorption probability corresponding to the $\lambda_{N-1} \rightarrow \lambda_N$ transition

$$P_{\lambda_{N-1} \rightarrow \lambda_N}(\omega) = \frac{2\pi}{\hbar} |H'_{\lambda_N \lambda_{N-1}}|^2 \delta(\mathcal{E}_{\lambda_N} - \mathcal{E}_{\lambda_{N-1}} - \hbar\omega). \quad (20)$$

It describes the many-exciton optical response of our QD structure, i.e., the probability of creating a new exciton in the presence of $N-1$ Coulomb-correlated electron-hole pairs.

1. Excitonic absorption

As a starting point, let us consider the so-called excitonic response, i.e., the optical response of our carrier system for the $0 \rightarrow 1$ transition. In this case, the initial ($N=0$) state is the (electron-hole) vacuum state $|0\rangle$, while the final ($N=1$) state $|\lambda_1\rangle$ corresponds to a Coulomb-correlated electron-hole pair, i.e., an exciton. Combining Eqs. (10) and (11), for $N=1$ we have

$$|\lambda_1\rangle = \sum_{l_1} U^{\lambda_1}_{l_1} c^\dagger_{i_1} d^\dagger_{j_1} |0\rangle, \quad (21)$$

where $l_1 = i_1, j_1$ denotes the single-particle electron-hole basis for $N=1$.

The excitonic-absorption probability is then given by Eq. (20) with $N=1$:

$$P^{\mathrm{ex}}_{\lambda_1}(\omega) = \frac{2\pi}{\hbar} |H'_{\lambda_1 0}|^2 \delta(\mathcal{E}_{\lambda_1} - \hbar\omega), \quad (22)$$

where

$$H'_{\lambda_1 0} = \langle \lambda_1 | \mathbf{H}' | 0 \rangle \quad (23)$$

is the matrix element of the light-matter Hamiltonian (14) for the $0 \rightarrow 1$ optical transition. Its explicit form is given in Appendix C. The excitonic spectrum is finally obtained by summing the absorption probability in Eq. (22) over all possible final states $|\lambda_1\rangle$:

$$A^{\mathrm{ex}}(\omega) = \sum_{\lambda_1} P^{\mathrm{ex}}_{\lambda_1}(\omega). \quad (24)$$

2. Biexcitonic absorption

Let us now come to the so-called biexcitonic response, i.e., the optical response corresponding to the $1 \rightarrow 2$ transition. In this case, the initial ($N=1$) state coincides with the excitonic state $|\lambda_1\rangle$ in Eq. (21), while the final ($N=2$) state $|\lambda_2\rangle$ corresponds to two Coulomb-correlated electron-hole pairs, i.e., a biexciton. Combining again Eqs. (10) and (11), for $N=2$ we get

$$|\lambda_2\rangle = \sum_{l_2} U^{\lambda_2}_{l_2} c^\dagger_{i_1} d^\dagger_{j_1} c^\dagger_{i_2} d^\dagger_{j_2} |0\rangle, \quad (25)$$

where $l_2 \equiv i_1 j_1, i_2 j_2$ denotes the single-particle electron-hole basis for $N=2$.

The excitonic-absorption probability is then given by Eq. (20) with $N=2$:

$$P^{\mathrm{biex}}_{\lambda_1 \rightarrow \lambda_2}(\omega) = \frac{2\pi}{\hbar} |H'_{\lambda_2 \lambda_1}|^2 \delta(\mathcal{E}_{\lambda_2} - \mathcal{E}_{\lambda_1} - \hbar\omega), \quad (26)$$

where

$$H'_{\lambda_2 \lambda_1} = \langle \lambda_2 | \mathbf{H}' | \lambda_1 \rangle \quad (27)$$

is the matrix element of the light-matter Hamiltonian (14) for the $1 \rightarrow 2$ optical transition. Its explicit form is given again in Appendix C.

The biexcitonic spectrum is finally obtained by summing the absorption probability in Eq. (26) over all possible final states $|\lambda_2\rangle$:

$$A^{\mathrm{biex}}_{\lambda_1}(\omega) = \sum_{\lambda_2} P^{\mathrm{biex}}_{\lambda_1 \rightarrow \lambda_2}(\omega). \quad (28)$$

We stress that, contrary to the excitonic spectrum in Eq. (24), the biexcitonic spectrum A^{biex} is a function of the initial excitonic state λ_1.

Equations (22) and (26) will be employed in Sec. III to investigate the electro-optical response of single as well as coupled QD structures. However, for the case of ultrafast optical excitation and strong light-matter coupling, the above perturbation-theory picture can no longer be applied, and the

time evolution of our many-body state $|\psi(t)\rangle$ can be obtained by solving the time-dependent Schrödinger equation in Eq. (16). We stress that, contrary to the many-exciton absorption probability in Eq. (20), the number of excitons, i.e.,

$$N(t)=\langle\Psi(t)|\mathbf{N}_e|\Psi(t)\rangle=\langle\Psi(t)|\mathbf{N}_h|\Psi(t)\rangle, \tag{29}$$

is a continuous function of time and changes according to the specific ultrafast laser-pulse sequence considered.

D. Interaction with environmental degrees of freedom

Let us finally come to the interaction of the carrier subsystem with various environmental degrees of freedom, such as phonons, plasmons, etc. They will not be treated explicitly; instead, we shall adopt a statistical description of the carrier subsystem in terms of its density-matrix operator

$$\rho(t)=\overline{|\Psi(t)\rangle\langle\Psi(t)|}, \tag{30}$$

the overbar denoting a suitable ensemble average.[22] Its time evolution can be schematically written as

$$\frac{d}{dt}\rho(t)=\frac{d}{dt}\rho(t)\bigg|_{\mathbf{H}}+\frac{d}{dt}\rho(t)\bigg|_{\mathrm{env}}. \tag{31}$$

The first term describes the deterministic evolution induced by the carrier Hamiltonian **H** according to the well-known Liouville–von Neumann equation

$$\frac{d}{dt}\rho(t)\bigg|_{\mathbf{H}}=\frac{1}{i\hbar}[\mathbf{H},\rho(t)], \tag{32}$$

while the second one describes a nonunitary evolution,[23] due to energy-relaxation and dephasing processes. The latter will be treated within the standard T_1T_2 model (see Sec. IV B).

As for the case of the Schrödinger equation (16), it is convenient to describe the density-matrix operator ρ—as well as its time evolution—within our Coulomb-correlated N-pair basis. By combining Eqs. (17) and (30), we get

$$\rho_{\lambda_N\lambda'_{N'}}(t)=\overline{a_{\lambda_N}(t)a^*_{\lambda'_{N'}}(t)}: \tag{33}$$

the density matrix in the λ representation is bilinear in the state coefficients a_{λ_n} in Eq. (17).

E. The excitonic picture

As discussed in Sec. II B, the generic Coulomb-correlated N-pair state $|\lambda_N\rangle$ can be written as a linear combination [see Eq. (11)] of the noninteracting electron-hole basis states in Eq. (10). Such single-particle picture is used to compute Coulomb-correlated N-pair states and energy levels via the exact-diagonalization approach described in Appendix C. However, it is often convenient to adopt—instead of a single-particle description—an excitoniclike picture, i.e., a quasiparticle number representation based on Coulomb-coupled electron-hole pairs. The aim of this section is (I) to show that, in general, such an excitonic description is not possible, and (II) to identify the basic requirements needed for such a quasiparticle number representation and therefore for QIC processing.

To this end, let us introduce the following set of excitonic creation operators

$$|\lambda_1\rangle=X^\dagger_{\lambda_1}|0\rangle, \tag{34}$$

where, as usual, $|0\rangle$ denotes the electron-hole vacuum state and λ_1 is the label for the generic excitonic ($N=1$) state. By comparing Eq. (21) with the above definition, we can write these excitonic operators in terms of the electron and hole operators, i.e.,

$$X^\dagger_{\lambda_1}=\sum_{ij}U^{\lambda_1}_{ij}c^\dagger_i d^\dagger_j. \tag{35}$$

Moreover, in view of the unitary character of the transformation U, we get

$$c^\dagger_i d^\dagger_j=\sum_{\lambda_1}U^{\lambda_1}_{ij}{}^* X^\dagger_{\lambda_1}. \tag{36}$$

If we now consider the explicit form of the noninteracting basis states in Eq. (10), the generic N-pair many-body state (11) can formally be written as

$$|\lambda_N\rangle=\sum_{\{\lambda_1\}}C^{\lambda_N}_{\{\lambda_1\}}|\{\lambda_1\}\rangle \tag{37}$$

with

$$|\{\lambda_1\}\rangle=\prod_{\lambda_1}X^\dagger_{\lambda_1}|0\rangle. \tag{38}$$

The expansion in Eq. (37) would suggest to define a sort of excitonic number representation in terms of the N-pair states $|\{\lambda_1\}\rangle$. We stress that, in general, this is not possible. The point is that, in general, *the set of states in Eq. (38) do not constitute a basis for our N-pair Hilbert subspace*. This is intimately related to the fact that—contrary to electron and hole creation and destruction operators—the excitonic operators in Eq. (35) do not obey canonic commutation relations. In general, the commutator

$$\mathcal{C}_{\lambda_1,\lambda'_1}:=[X_{\lambda_1},X^\dagger_{\lambda'_1}] \tag{39}$$

is itself an operator. This clearly prevents the introduction of number operators, and, therefore, of a genuine quasiparticle number representation.

As will be discussed in Sec. IV, two basic requirements are needed to perform quantum information processing: (i) the tensor-product structure of the ''computational space'' considered and (ii) the SU(2) character of the raising/lowering operators acting on our computational subsystems, known as ''qubits.'' The main question is thus to study if—and in which conditions—the Coulomb-correlated electron-hole system discussed so far may act as quantum hardware, i.e., may be used to perform quantum information process-

ing. This requires to identify a set of independent degrees of freedom, qubits, with a SU(2) character, the one of spin-$\frac{1}{2}$ systems.

As a starting point, one should then check if there exist a set of independent excitonic degrees of freedom; this corresponds to verify that for any pair of excitonic states λ_1 and λ_1' the commutator of Eq. (39) is equal to zero.

Let us now discuss the tensor product structure of our computational subspace. To this end let us consider again the case of two qubits *a* and *b*. Generally speaking, we know that the Hilbert space of a bipartite system is $\mathcal{H}_a \otimes \mathcal{H}_b$, where $\mathcal{H}_{a/b}$ are the Hilbert spaces of the individual qubits. This means that if $\{|l_a\rangle\}$ is an orthonormal basis set for $\mathcal{H}_a$ and $\{|l_b\rangle\}$ is an orthonormal basis set for $\mathcal{H}_b$, then $\{|l_a\rangle \otimes |l_b\rangle\}$ is a basis set for the whole computational space. What one needs to test is the possibility of writing the many-body ground state—corresponding in this case to a biexcitonic state λ_2–as the product of two independent excitonic states λ_1^a and λ_1^b. This corresponds to verify that

$$\langle \lambda_2 | (|\lambda_1^a\rangle |\lambda_1^b\rangle) = 1. \tag{40}$$

Provided that the above requirements are fulfilled, let us now focus on the single qubit, i.e., on one of the independent excitonic states λ_1. In this case, we want to check that the exciton creation/annihilation operators introduced in Eq. (34) obey usual SU(2) commutation relations. More specifically, we are interested in defining the *z*-component pseudospin operator $S^z_{\lambda_1}$ as

$$S^z_{\lambda_1} := \frac{1}{2} \mathcal{C}_{\lambda_1,\lambda_1}. \tag{41}$$

In order to check that this is really a *z*-component spin operator, we should verify that its average value over our many-body state is either plus or minus one. Deviations from this ideal scenario can be regarded as a measure of the leakage from our computational space due to the presence of external, i.e., noncomputational, excitonic states. In Sec. IV we shall show that for prototypical GaAs-based quantum-dot molecules all the above requirements are well fulfilled and our excitonic system can indeed be used as quantum hardware.

III. ELECTRO-OPTICAL RESPONSE OF SEMICONDUCTOR QUANTUM DOTS

In this section we shall analyze the electro-optical properties, i.e., the optical response in the presence of a static electric field **F**, of single as well as coupled QD structures. While the light-matter interaction is described by the Hamiltonian $\mathbf{H}'$ in Eq. (14), the presence of a static field **F** can be accounted for by adding to the confinement potential $V_c^{e/h}$ in Eq. (1) the corresponding scalar-potential term

$$V_c^{e/h}(\mathbf{r}) \rightarrow V_c^{e/h}(\mathbf{r}) \pm e\mathbf{F}\cdot\mathbf{r}. \tag{42}$$

Here, the $\pm$ sign refers, respectively, to electrons and holes. As discussed below, this sign difference will give rise to exciton-exciton coupling and significant field-induced energy renormalizations.

Within the usual envelope-function picture,[19] the single-particle properties of our quasi 0D structure are described by the Schrödinger equation in Eq. (1). Similar to the case of semiconductor quantum wires,[24] a quantitative analysis of the whole single-particle spectrum requires a direct numerical solution of Eq. (1); this can be performed using a fully 3D plane-wave expansion, as described in Ref. 25 and briefly recalled in Appendix A.

If, in contrast, our interest is limited to the low-energy range only, for most of the QD structures realized so far the carrier confinement can be described as the sum of two potential profiles, one acting along the growth (or perpendicular) direction and one affecting the in-plane (or parallel) coordinates only:

$$V_c^{e/h}(\mathbf{r}) = V_\perp^{e/h}(r_\perp) + V_\parallel^{e/h}(\mathbf{r}_\parallel). \tag{43}$$

As a consequence, the 3D carrier envelope function $\psi_{i/j}$ can be factorized according to

$$\psi_{i/j}(\mathbf{r}) = \psi^\perp_{i_\perp/j_\perp}(r_\perp)\psi^\parallel_{i_\parallel/j_\parallel}(\mathbf{r}_\parallel) \tag{44}$$

and the single-particle spectrum is the sum of the parallel and perpendicular ones:

$$\epsilon_{i/j} = \epsilon^\perp_{i_\perp/j_\perp} + \epsilon^\parallel_{i_\parallel/j_\parallel}. \tag{45}$$

In this case, the original 3D problem is reduced to the solution of two independent Schrödinger equations, along the growth direction and within the parallel plane. This can be still performed employing the plane-wave-expansion approach described in Appendix A.

For most of the state-of-the-art QD structures we have strong confinement (few nanometers) along the growth direction, while the in-plane confinement potential $V_\parallel^{e/h}$ is much weaker. Moreover, as far as the low-energy region is concerned, the in-plane confinement is well described in terms of a 2D parabolic potential. For this case the Schrödinger equation within the 2D parallel subspace can be solved analytically—also in the presence of the static field **F** (see Appendix A)—and thus the problem reduces to a numerical solution of the Schrödinger equation along the perpendicular direction. The analysis of the electro-optical response of semiconductor quantum dots presented in the remainder of this section is based on this parabolic-confinement model, whose derivation and validity limits are discussed in Appendix A.

A. Single QD structure

Let us start our analysis by considering the case of a single QD structure in the presence of an in-plane static electric field: $\mathbf{F} = (F_\parallel, F_\perp = F, 0)$. Within the parabolic-confinement model previously introduced (see also Appendix A), the quasi-0D carrier confinement for both electrons and holes is described by an in-plane parabolic potential $V_\parallel^{e/h}$

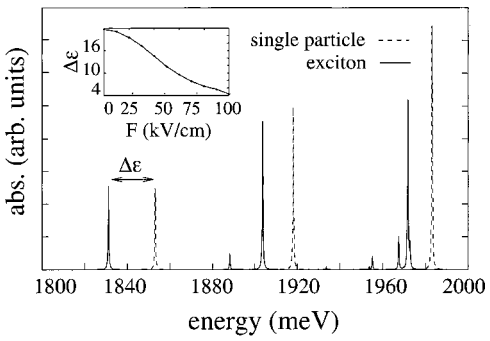

FIG. 1. Single-particle (dashed curve) and excitonic absorption spectra (solid curve) in the field-free case ($F=0$). The inset shows how the exciton binding energy $\Delta\mathcal{E}$ is reduced as the in-plane electric field F increases.

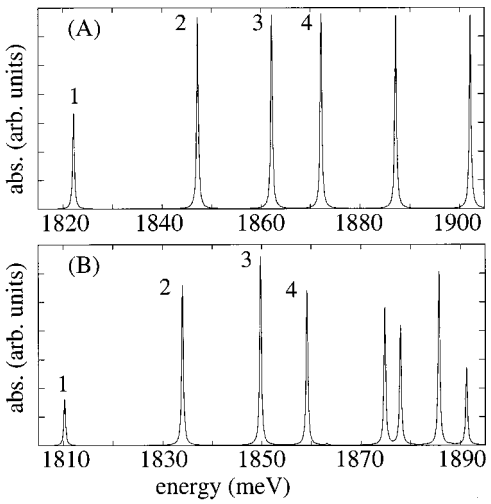

FIG. 2. Single-particle (a) and excitonic absorption spectra (b) for an in-plane field $F=50$ kV/cm. The excitonic spectrum in (b)—apart from a rigid shift due to Coulomb interaction—is now comparable to the single-particle one. Here, numbers from 1 to 4 identify corresponding transitions in each spectrum.

[see Eq. (A5)] plus a squarelike potential $V_{\perp}^{e/h}$ corresponding to the interface band offset along the growth direction.

As a starting point, we have considered an ideal QD structure characterized by the following material and confinement parameters for electrons and holes: effective mass $m_e=0.05m_\circ$, $m_h=0.08m_\circ$, and parabolic-confinement energy $\hbar\omega_e=40$ meV, $\hbar\omega_h=25$ meV; the well width is $w=50$ Å and the static dielectric constant [see Eq. (B3)] has been taken to be $\varepsilon_0=12$. Within this ideal QD model, the squarelike potential profile along the growth direction is characterized by an infinite barrier height, i.e., $\Delta_{e/h}\gg\hbar^2\pi^2/2m_{e/h}w^2$. By choosing the above material and confinement parameters for electrons and holes, we deal with a very special case for which the set of electron and hole single-particle envelope functions ψ^e and ψ^h coincide. Indeed, the in-plane spatial extension α in Eq. (A11) is the same for electrons and holes. Moreover, we shall discuss how this symmetry, not present in a realistic QD structure (see below), is related to special features in the optical response of the system (''hidden symmetry''), as described in Ref. 13.

Due to the strong perpendicular carrier confinement, for both electrons and holes we deal with a single localized state; therefore, the low-energy single-particle spectrum is simply given by a sequence of equally spaced discrete levels corresponding to the 2D parabolic confinement [see Eq. (A12)]. This scenario is not affected by the presence of the in-plane static field F, which manifests itself only through an overall redshift $\Delta\mathcal{E}$ of the single-particle spectrum, known as Stark shift [see Eq. (A9)].

In the absence of Coulomb interaction, both the excitonic and the biexcitonic absorption spectra [see Eqs. (24) and (28)] will exhibit optical transitions connecting the above single-particle energy levels. As usual, their amplitude is dictated by the corresponding optical matrix elements, i.e., oscillator strength, as well as by the combined state degeneracy, i.e., joint density-of-states (DOS).

Figures 1 and 2(b) show the excitonic-absorption spectrum for $F=0$ and $F=50$ kV/cm, respectively. Moreover, the excitonic-absorption spectra are compared to the single-particle ones, i.e., the ones evaluated in the absence of Coulomb interaction, which respectively correspond to the dashed curves in Figs. 1 and 2(a). As already pointed out, in this case the optical transitions connect the equally spaced single-particle electron and hole states.

As discussed in Appendix A, for $F=0$ the only allowed optical transitions are those conserving the envelope function total angular momentum, i.e., $m=-m'$ [see Eq. (A20)]; moreover, due to the special symmetry between electrons and holes previously discussed, we have $n_\epsilon=n'_\epsilon$ [see Eq. (A12)]. Their amplitude is dictated by the joint state degeneracy, which for the single-particle case (see dashed line) is given by $(n_\epsilon+1)$. In contrast, for finite values of the in-plane static field F [see part (a) in Fig. 2], the above selection rules are relaxed (see Appendix A) and we deal with new optical transitions corresponding to $m+m'\neq 0$ and $n_\epsilon\neq n'_\epsilon$, not present in the field-free case. Moreover, in the presence of the static field the spectra exhibit a significant reduction in oscillator strength. This is ascribed to a reduction of the in-plane overlap between electrons and holes [see Eq. (A18)], due to the charge separation induced by the applied field [see Eq. (A8)]. This can be clearly seen in Fig. 4, where we show the single-particle electron and hole ground-state charge distributions (dashed curves) corresponding to the single-particle spectra of Fig. 2. For $F=0$ (see Fig. 3) the electron and hole parabolic-potential minima coincide and, therefore, the two charge distributions exhibit the same symmetry center. In contrast, in the presence of the in-plane field F the two potential minima are shifted toward different directions. This, in turn, induces an electron-hole charge separation, as clearly shown in Fig. 4. Such charge displacement—which corresponds to the formation of an in-plane electrical dipole—is responsible for the oscillator-strength reduction in Fig. 2 previously discussed.

Let us now come to the Coulomb-correlated case (see solid curves in Figs. 1 and 2 and Figs. 3 and 4). In the presence of Coulomb interaction—which for the excitonic case ($N=1$) corresponds to electron-hole attraction—the

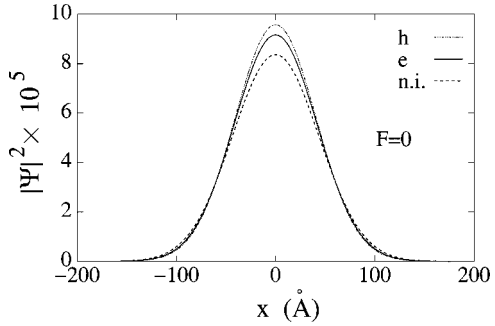

FIG. 3. Effective electron and hole charge distribution for the ground-state exciton in the field-free case. The three curves correspond to noninteracting (Ni) as well as to Coulomb-correlated e-h pairs as indicated.

main effect is a global redshift of the Coulomb-correlated spectrum compared to the single-particle one. More precisely, for $F=0$ we find a relatively strong redshift of the lowest optical transition (of about 20 meV). For higher transitions this effect is reduced, which can be understood considering that high-energy states are characterized by an increasing spatial extension and, therefore, by a larger average distance between electrons and holes. Moreover, the Coulomb-correlated spectrum exhibits a transfer of oscillator strength toward low energies between quasidegenerate optical transitions. This scenario is well established, and characterizes also systems of higher dimensionality, such as quantum wells and wires.[2,24] For increasing values of the applied field we have a progressive reduction of the excitonic redshift as well as of the oscillator-strength transfer, i.e., of the electron-hole attraction. This is confirmed by the inset of Fig. 1, where the exciton binding energy is reported as a function of the applied field.

In order to better understand the physical origin of this field-dependent behavior, we have carried on a detailed investigation of the excitonic wave function projected into the electron and hole subspaces. More precisely, by rewriting Eq. (21) in the coordinate representation, the two-body excitonic wave function is given by

$$\Psi_\lambda^{\mathrm{ex}}(\mathbf{r}_e,\mathbf{r}_h)=\sum_{ij} U_{ij}^\lambda \psi_i(\mathbf{r}_e)\psi_j(\mathbf{r}_h). \tag{46}$$

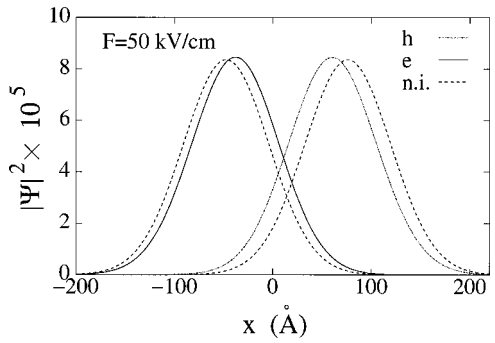

FIG. 4. Same as in Fig. 3 but for an in-plane field $F=50$ kV/cm.

The square modulus of Ψ^{ex} will then describe the conditional probability of finding the electron with coordinate $\mathbf{r}_e$ and the hole with coordinate $\mathbf{r}_h$. If we now integrate such quantity over one of the two coordinates we get

$$f_\lambda^e(\mathbf{r}_e)=\int |\Psi_\lambda^{\mathrm{ex}}(\mathbf{r}_e,\mathbf{r}_h)|^2 d\mathbf{r}_h=\sum_{ii',j} U_{ij}^{\lambda *} U_{i'j}^{\lambda} \psi_i^*(\mathbf{r}_e)\psi_{i'}(\mathbf{r}_e) \tag{47}$$

and

$$f_\lambda^h(\mathbf{r}_h)=\int |\Psi_\lambda^{\mathrm{ex}}(\mathbf{r}_e,\mathbf{r}_h)|^2 d\mathbf{r}_e=\sum_{i,jj'} U_{ij}^{\lambda *} U_{ij'}^{\lambda} \psi_j^*(\mathbf{r}_h)\psi_{j'}(\mathbf{r}_h). \tag{48}$$

The quantity $f_\lambda^{e/h}$ can be regarded as an effective single-particle probability distribution, which accounts for the electron-hole correlation described by the excitonic wave function in Eq. (46). In the absence of Coulomb correlation the transformation U reduces to the identity ($U_{ij}^\lambda=\delta_{\lambda,ij}$) and the effective single-particle distributions $f_\lambda^{e/h}$ coincide with the square modulus of the single-particle wave functions of electrons and holes, i.e., $f_i^e(\mathbf{r}_e)=|\psi_i(\mathbf{r}_e)|^2$, $f_j^h(\mathbf{r}_h)=|\psi_j(\mathbf{r}_h)|^2$.

The effective charge distributions for electrons and holes—defined, respectively, in Eqs. (47) and (48)—are plotted in Figs. 3 and 4 for the ground-state-exciton case. As expected, in the presence of Coulomb correlation the charge distribution deviates from the corresponding Coulomb-free case (dashed curves). For $F=0$ (Fig. 3) the average distance between electrons and holes is very limited, which leads to a strong exciton binding (see Fig. 1). For increasing values of the applied field (Fig. 4) we see again an increasing charge separation. However, the effect is now reduced, compared to the Coulomb-free case (see dashed curves). This is due to the competition between the displaced parabolic potentials and the electron-hole Coulomb attraction (see also Fig. 12 in Sec. III C). The latter is progressively reduced due to a significant increase of the electron-hole average distance (see again Fig. 4). This also explains the reduction of the excitonic binding energy reported as inset in Fig. 1.

The analysis presented so far suggests that the behavior of the system is governed by the following three characteristic lengths.

(i) The radial extension α of the parabolic ground state, which in this case is the same for electrons and holes [see Eq. (A11)].

(ii) The excitonic Bohr radius

$$a^{\mathrm{ex}}=\frac{\hbar^2\varepsilon_0}{e^2\mu}, \tag{49}$$

where μ is the reduced electron-hole mass.

(iii) The total electron-hole displacement $d=|\mathbf{d}_\parallel^h-\mathbf{d}_\parallel^e|$ [see Eq. (A8)].

Generally speaking, when $\alpha \ll a^{\mathrm{ex}}$ we are in the so-called strong-confinement limit: the carrier confinement is dictated by the single-particle parabolic potential only, which implies that the wave function of the excitonic ground state coincides with the product of the electron and hole single-particle wave

functions, i.e., the expansion in Eq. (46) contains just one term. In the opposite case, called weak-confinement limit ($\alpha \gg a^{\mathrm{ex}}$), the excitonic wave function depends on the relative coordinate only and resembles the 2D hydrogen-atom solution.

For the case under investigation the situation is as follows. In the field-free case ($d=0$), the excitonic Bohr radius ($a^{\mathrm{ex}} \simeq 200$ Å), is of the same order of the electron and hole ground-state radial extension ($\alpha \simeq 60$ Å), which implies that the exciton wave function deviates from the product of the corresponding single-particle states. This is confirmed by the Coulomb-correlated carrier distribution of Fig. 3, compared to the Coulomb-free one (dashed curve). However, we are not very far from the ideal strong-confinement limit previously discussed; Indeed, our numerical analysis has shown that the single-particle expansion in Eq. (46) can be limited to a relatively small number (6×6) of electron-hole states. For increasing values of the applied field—and, therefore, of the charge displacement d—the average distance between electrons and holes increases, thus reducing Coulomb-correlation effects. This is confirmed by the absorption spectra in Fig. 2 as well as by the carrier distributions in Fig. 4, where the difference between Coulomb-correlated and Coulomb-free results is significantly reduced. We can therefore conclude that the presence of an in-plane static field F induces a net electron-hole charge separation, which leads to a significant suppression of electron-hole Coulomb correlation.

Let us now move to the biexcitonic response of our ideal QD system. As discussed in Sec. II C, contrary to the excitonic case investigated so far, the latter depends on the spin configuration of both initial ($N=1$) and final ($N=2$) Coulomb-correlated states. More precisely, due to the spin selection rules in the light-matter interaction Hamiltonian, we deal with two relevant cases only: the parallel- and the antiparallel-spin one.

Let us consider first the antiparallel-spin configuration. In this case both excitons can occupy the low-energy orbital state. Figure 5 shows the biexcitonic spectrum (dashed curve) compared to the excitonic one (solid curve) for $F=30$ kV/cm. We can clearly identify a biexcitonic transition (see first peak of the dashed curve), which is blueshifted with respect to the ground-state excitonic transition (see first peak of the solid curve). This energy renormalization is known as *biexcitonic shift*[4]

$$\Delta\mathcal{E}=\mathcal{E}_{\lambda_2}-\mathcal{E}_{\lambda_1}-\mathcal{E}_{\lambda_1'}. \tag{50}$$

This positive energy shift can be understood as follows: the applied field induces for both excitons the same charge separation (see Fig. 4) which results in a repulsive dipole-dipole coupling. This is confirmed by the field-dependent behavior of the biexcitonic splitting $\Delta\mathcal{E}$ shown in the inset in Fig. 5.

Moreover, as shown in the inset, in the field-free case, the dot behaves as an artificial atom and the energy to add an exciton in a shell is, up to the first order in the Coulomb interaction, independent of the shell occupation.[17] Indeed, within first-order perturbation theory, when $F=0$ the two excitons occupy the same spherically symmetric orbital

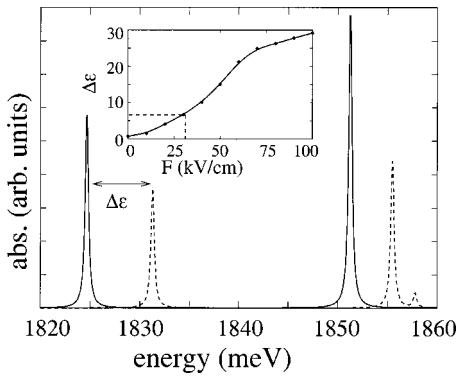

FIG. 5. Excitonic (solid curve) and biexcitonic optical response (dashed curve) for the antiparallel-spin configuration in the presence of an in-plane electric field $F=30$ kV/cm. The inset shows the biexcitonic splitting $\Delta\mathcal{E}$ as a function of the in-plane field F. Notice that for $F=0$, the latter becomes very small ($\Delta\mathcal{E}=0.7$ meV), which is due to the special symmetry of the QD structure considered: $\alpha_e=\alpha_h$ (see text).

ground state and for an ideal structure as the one we are considering, the biexcitonic splitting is exactly zero, because in this case the various attractive and repulsive Coulomb interactions cancel exactly.[13] This can be understood as follows. In the strong-confinement limit—which is not far from the regime considered here—and for antiparallel spins, the biexcitonic splitting can be very well approximated by the noninteracting single-particle probability distributions $f_0^e=|\psi_0^e|^2$ and $f_0^h=|\psi_0^h|^2$ only, i.e.,

$$\Delta\mathcal{E}=\frac{e^2}{\varepsilon_0}\int d\mathbf{r}\int d\mathbf{r}'\frac{\Delta f(\mathbf{r})\Delta f(\mathbf{r}')}{|\mathbf{r}-\mathbf{r}'|}, \tag{51}$$

where $\Delta f=f_0^e-f_0^h$ is the difference between the electron and hole single-particle probability densities. Due to the special symmetry of the ideal QD structure under investigation, in the field-free case we have $\Delta f=0$ and the biexcitonic splitting is zero as well.

As already pointed out, in the QD structure under investigation we are not far from the strong confinement limit. However, since our calculation of the biexcitonic splitting is nonperturbative, we get, even in the field-free case, a nonvanishing $\Delta\mathcal{E}$. This small, but not negligible biexcitonic splitting [$\Delta\mathcal{E}(F=0)=0.7$ meV, see inset in Fig. 5] measures the Coulomb-interaction contribution, underlying that the real ground-state biexcitonic wave function has contributions also from higher-level single-particle states. This value is compatible with the one given in Ref. 4.

We shall now show that the above field-free behavior is due to the special choice of material and confinement parameters of the ideal QD structure investigated so far. To this aim, let us now move to the case of a realistic semiconductor macroatom. As prototypical system let us consider a GaAs/AlAs QD structure characterized by the following material parameters: effective masses $m_e=0.067m_0$ and $m_h=0.34m_0$, conduction- and valence-band offsets $\Delta_e=1$ eV and $\Delta_h=0.58$ eV, parabolic-confinement energies $\hbar\omega_e$

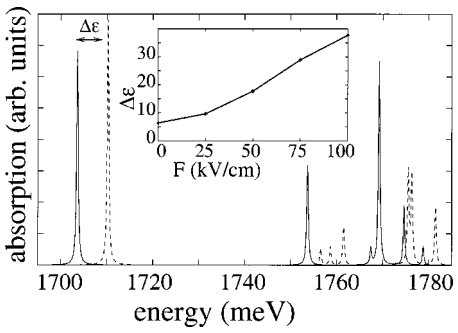

FIG. 6. Excitonic (solid curve) and biexcitonic optical response (dashed curve) of a realistic QD structure for the antiparallel-spin configuration in the field-free case. The inset shows the biexcitonic splitting $\Delta\mathcal{E}$ as a function of the in-plane field F. Opposite to the symmetric case previously considered (see Fig. 5), in this more realistic case the spatial extension for electrons and holes as well as their Coulomb matrix elements are considerably different; this is the physical origin of the positive biexcitonic shift in the field-free case (see text).

$=30\,\mathrm{meV}$ and $\hbar\omega_h=24\,\mathrm{meV}$, well width $w=50\,\text{Å}$, and static dielectric constant $\varepsilon_0=12.1$.

Figure 6 shows again the comparison between excitonic (solid curve) and biexcitonic spectrum (dashed curve) for the antiparallel case in the field-free case. As we can see, contrary to the result in Fig. 5, we now deal with a significant biexcitonic splitting $\Delta\mathcal{E}$ also in the absence of the in-plane field (see inset in Fig. 6). Indeed, for any realistic QD structure we deal with different spatial extensions α_e and α_h of the electron and hole single-particle in-plane ground states. In Fig. 7 we report the electron and hole single-particle charge distributions f^e and f^h (solid curves) as well as their difference Δf (dashed curve). As anticipated, due to the different material and confinement parameters, the charge distributions for electrons and holes do not coincide anymore. This, in turn, gives rise to local violations of charge neutrality, i.e., $\Delta f\neq 0$, and therefore to a nonvanishing biexcitonic shift [see Eq. (51)]. We finally stress that the presence of the in-plane static field leads to a further increase of $\Delta\mathcal{E}$ (see inset in Fig. 6).

Let us now move to the parallel-spin configuration. In this case we study the probability of creating a second exciton in

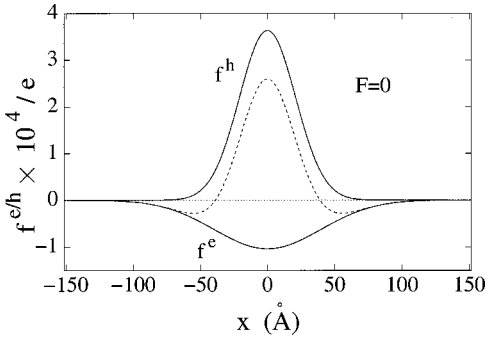

FIG. 7. Effective electron and hole charge distributions for the ground-state exciton in the field-free case (solid curves) as well as their difference (dashed curve). Due to the realistic QD parameters considered, the charge neutrality is violated: $\Delta f\neq 0$ (see text).

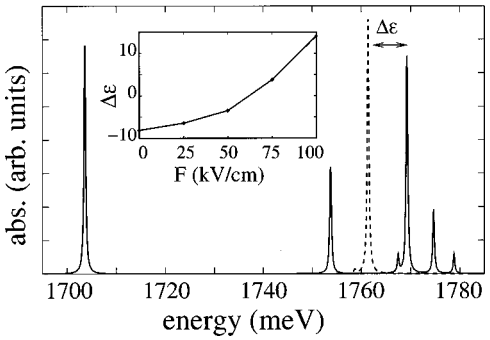

FIG. 8. Excitonic (solid curve) and biexcitonic optical response (dashed curve) of a realistic QD structure for the parallel-spin configuration in the field-free case. The inset shows the biexcitonic splitting $\Delta\mathcal{E}$ as a function of the in-plane field F. As can be seen from the spectra, the latter is now negative for $F=0$. However, it becomes positive at high fields (see text).

the dot with the same spin orientation of the first one. Due to the Pauli exclusion principle, the two excitons are not allowed to occupy the same exciton state. As already pointed out [see Eq. (28)], the biexcitonic spectrum of the system depends on its initial excitonic state $|\lambda_1\rangle$. In Fig. 8 we compare the biexcitonic spectrum (dashed curve) with the corresponding excitonic spectrum (solid curve) for the field-free case. Here, the biexcitonic spectrum has been computed assuming, as initial state $|\lambda_1\rangle$, the excitonic ground state. Let us focus on the low-energy part of the spectrum: as expected, due to the Pauli principle, the exciton ground state is forbidden to the second exciton, which can occupy any other high-energy state. Contrary to the antiparallel case (see inset in Fig. 6), we now deal with a negative biexcitonic shift $\Delta\mathcal{E}$, i.e., the lowest biexcitonic transition (solid curve) is red-shifted compared to the corresponding excitonic one (second peak of the dashed curve). As discussed in Ref. 25, such energy renormalization (in this case of the order of 10 meV) can be ascribed to the attractive dipole-dipole interaction between the two excitons in the dot. Indeed, due to their different orbital quantum numbers λ_1 and λ_1'—and thus to their different spatial charge distributions—they exhibit significant Coulomb coupling. Contrary to the antiparallel-spin case previously discussed (see inset in Fig. 6), now the presence of an in-plane static field F leads to a reduction and eventually to an inversion of the biexcitonic shift (see inset in Fig. 8). This can be understood as follows: the application of the in-plane field leads to a progressive reduction of the attractive, i.e., spatially antiparallel, dipole-dipole Coulomb coupling; for high fields this is transformed into a repulsive, i.e., spatially parallel, dipole-dipole interaction, and therefore to a positive biexcitonic splitting. The transition from red biexcitonic shifts to blue ones, occurs when the displacement induced by the electric field becomes of the same order or bigger than the excitonic Bohr radius.

B. Coupled QD structure

Let us now consider the case of a semiconductor macromolecule, i.e., a coupled QD structure. In particular, as prototypical system we shall investigate the GaAs/AlAs coupled

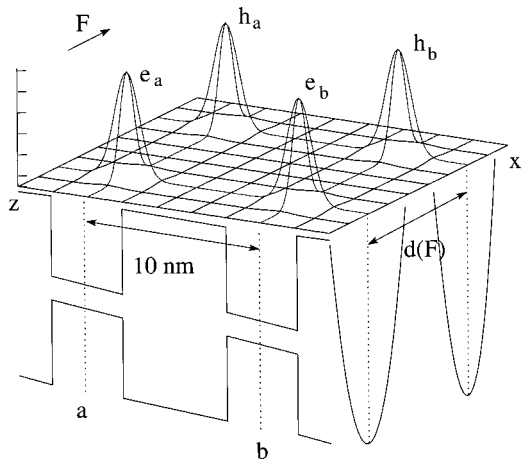

FIG. 9. Schematic representation of the electron and hole charge distribution as well as of the confinement potential profile in our Coulomb-coupled QD structure. The latter is tailored in such a way to allow for an energy-selective creation/destruction of bound electron-hole pairs in dots *a* and *b*. Moreover, the interdot barrier width ($w \sim 50$ Å) is such to prevent single-particle tunneling and at the same time to allow for significant interdot Coulomb coupling (see text).

QD structure schematically depicted in Fig. 9. The material and confinement parameters are the same of the realistic single-QD structure previously investigated (see Figs. 6, 8, and 7): effective masses $m_e = 0.067 m_0$ and $m_h = 0.34 m_0$, conduction- and valence-band offsets $\Delta_e = 1$ eV and $\Delta_h = 0.58$ eV, parabolic-confinement energies $\hbar\omega_e = 30$ meV and $\hbar\omega_h = 24$ meV, static dielectric constant $\varepsilon_0 = 12.1$. The squarelike carrier confinement along the growth direction for electrons and holes is schematically depicted in Fig. 9 for our semiconductor macromolecule $a+b$. This is tailored in such a way to allow for an energy-selective creation/destruction of bound electron-hole pairs in dots *a* and *b*. Indeed, the width of wells *a* and *b* are slightly different, which corresponds to a blueshift of about 10 meV of the single-particle optical transitions of dot *b* with respect to the corresponding transition in dot *a*. We stress that such energy shift is also present in the absence of interdot tunneling and Coulomb coupling. Moreover, the interdot barrier width ($w \sim 50$ Å) is such to prevent single-particle tunneling and at the same time to allow for significant interdot Coulomb coupling. We stress that the geometrical and material parameters of the proposed prototypical structure in Fig. 9 are fully compatible with current QD growth and characterization technology.[4,26]

Let us discuss first the excitonic response of the *semiconductor macromolecule* $(a+b)$ in Fig. 9. The excitonic $(0 \rightarrow 1)$ optical spectrum in the presence of an in-plane electric field $F = 75$ kV/cm is shown in Fig. 10. Here, the Coulomb-correlated result (B) is compared to the Coulomb-free one (A). The scenario is very similar to the single-dot case previously investigated (see Fig. 1): for relatively strong values of the applied field, apart from a rigid redshift, the Coulomb-correlated result is very similar to the Coulomb-free one. Here, the two lowest optical transitions correspond to the formation of direct ground-state excitons in dot *a* and *b*, respectively (see Fig. 9). In contrast, the high-energy peaks

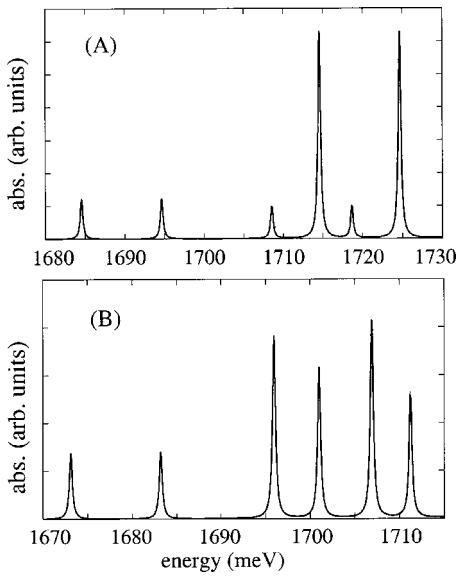

FIG. 10. Excitonic response of the array unit cell $(a+b)$ in Fig. 9 for an in-plane field $F = 75$ kV/cm. The Coulomb-correlated result in (b) is compared to the Coulomb-free one in (a).

correspond to optical transitions involving excited states of the in-plane parabolic potential. Due to the strong in-plane carrier confinement—compared to the relatively large electron-hole charge displacement—the two low-energy excitonic states are expected to closely resemble the corresponding single-particle ones.

Let us now come to the biexcitonic response of our semiconductor macromolecule. In view of the strong-confinement regime considered, we shall focus on the two ground-state excitons only. Moreover, since we are primarily interested in studying interdot Coulomb coupling, we shall consider the parallel-spin configuration.

In Fig. 11 the excitonic spectrum (solid curve) is compared to the biexcitonic one (dashed curve). The latter describes the generation of a second electron-hole pair in the presence of a previously created exciton $(1 \rightarrow 2$ optical tran-

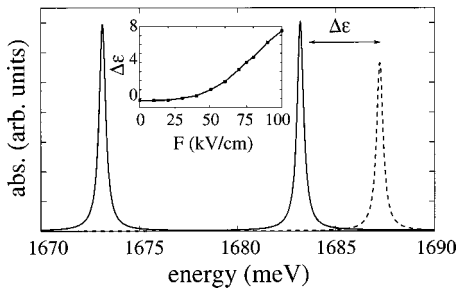

FIG. 11. Excitonic (solid curve) and biexcitonic spectrum (dashed curve) for an in-plane field $F = 75$ kV/cm. Due to the well-defined polarization of our laser source, the structure in the biexcitonic spectrum (dashed curve) corresponds to the formation of an exciton in dot *b* given an exciton in dot *a*. One obtains a similar structure in the biexcitonic spectrum, symmetrically blueshifted with respect to the excitonic transition in dot *a*, if one considers as initial state an exciton in dot *b*. The biexcitonic shift $\Delta\mathcal{E}$ as a function of the in-plane field *F* is also reported in the inset.

sitions). In particular, here the previously generated exciton is assumed to be in dot *a*. As for the single-dot case previously investigated (see Fig. 6), the crucial feature in Fig. 11 is the magnitude of the biexcitonic shift. For the QD structure under investigation we get energy splittings up to 8 meV (see inset in Fig. 11). This can be ascribed again to the in-plane static field F, which induces, in both dots, the excitonic dipole previously investigated (see Fig. 4). This, in turn, gives rise to significant interdot dipole-dipole coupling between adjacent excitonic states. The microscopic nature of such exciton-exciton coupling is the same of the Forster process exploited by Quiroga and Johnson[27] for the generation of entangled states in coupled QD's.

The physical origin of the biexcitonic shift $\Delta\mathcal{E}$ is qualitatively described in Fig. 9, where we show the effective spatial charge distribution of the two electrons (e_a and e_b) and holes (h_a and h_b) corresponding to the biexcitonic ground state in Fig. 11. As we can see, the charge separation induced by the static field increases significantly the average distance between electrons and holes, thus decreasing their attractive interaction. On the other hand, the repulsive terms are basically field independent. This is the origin of the positive energy difference $\Delta\mathcal{E}$ in Fig. 11.

Let us now investigate the possibility of using such QD molecules as quantum hardware for QIC processing. As discussed in Sec. II E, to this end a few basic requirements should be fulfilled. First of all, the operators for the two ground-state excitons in dots *a* and *b* should commute. By evaluating the average value (over the biexcitonic ground state) of the commutator in Eq. (39), this came out to be negligibly small, thus confirming that these are indeed independent degrees of freedom. Moreover, due to the relatively large interdot distance—compared to the spatial extension of the carrier wave functions along the growth direction—the biexcitonic ground state in Fig. 9 is expected to closely resemble the product of the two excitonic states in dots *a* and *b*. Indeed, for the coupled QD structure under investigation we find that the scalar product in Eq. (40) gives a value of 0.99, very close to 1. The product structure for the bipartite system Hilbert space is therefore very well achieved. It is worth noticing that, in the case in which the two excitonic states are localized on the same dot, e.g., in the ground and first excited states, one gets a smaller value of about 0.9. This is a clear indication that the tensor product structure for the many-body state is much better achieved in a coupled QD structure than in a single QD system, as the one proposed in Ref. 25.

Let us finally focus on the SU(2) character of our excitonic qubits. To this end, we have evaluated the average value (over the biexcitonic ground state) of the pseudospin operator S^z introduced in Eq. (41). By truncating the single-particle basis considering just the lowest energy level in each QD (strong-confinement limit), one gets $\langle\lambda_2|S^z_{\lambda_1}|\lambda_2\rangle=1$, thus confirming that the operators in Eqs. (39) and (41) are the generators of a SU(2) algebra. In contrast, far from the strong-confinement limit, we get a result which is of course dependent on how many single-particle states contribute to form an exciton. Therefore, if we calculate again the mean value of the commutator considering an enlarged single-particle basis set, we get deviations from the above ideal result. As anticipated in Sec. II E, this turns out to be a measure of the leakage of our qubit.

We can therefore conclude that ground-state excitonic transitions in our coupled QD molecule fulfill all the basic requirements for a semiconductor-based implementation of QIC processing. They can be used as computational degrees of freedom, i.e., qubits, and the standard pseudospin language can be employed.

C. A simplified model

In this section we shall present a simplified model able to properly describe excitonic binding as well as interdot biexcitonic coupling. Its analytical solution will allow for an extremely quick way of identifying suitable parameter sets needed to employ the above coupled QD structure as semiconductor-based hardware for QIC processing (see Sec. IV). As a starting point, let us consider again the typical single-QD structures of Sec. III A, whose single-particle confinement is modeled in terms of a boxlike potential of width *a* in the growth (or perpendicular) direction and a 2D parabolic potential in the in-plane (or parallel) directions. As previously discussed, this allows a factorization of the original 3D single-particle problem into a perpendicular and a parallel one [see Eqs. (44) and (45)]. However, in the presence of Coulomb interaction such factorization is, in principle, no longer possible.

More specifically, let us consider the single-exciton problem ($N=1$) in the presence of an in-plane electric field $\mathbf{F}$; this can be described by the two-body Hamiltonian

$$\mathbf{H}=\mathbf{H}^e(\mathbf{r}_e)+\mathbf{H}^h(\mathbf{r}_h)-\frac{e^2}{\varepsilon_0|\mathbf{r}_e-\mathbf{r}_h|}. \tag{52}$$

As discussed in Appendix A, the single-particle Hamiltonians for electrons and holes can be written in the compact form [see Eqs. (A2), (A6), and (A7)]:

$$\mathbf{H}^{e/h}(\mathbf{r})=-\frac{\hbar^2\nabla^2_{\mathbf{r}}}{2m_{e/h}}+V^{e/h}_{\perp}(r_{\perp})+\frac{1}{2}m_{e/h}\omega^2_{e/h}|\mathbf{r}_{\parallel}-\mathbf{d}^{e/h}_{\parallel}|^2+\Delta\epsilon_{e/h}. \tag{53}$$

Here, the presence of the applied field results in a displacement $\mathbf{d}^{e/h}_{\parallel}$ [see Eq. (A8)] of the parabolic-potential minimum as well as in a rigid energy shift $\Delta\epsilon_{e/h}$ [see Eq. (A9)]. We want to show that for all the QD structures previously investigated Eq. (52) can be approximated to an analytically solvable form, and important quantities as wave functions or biexcitonic shifts can be easily estimated with a good degree of accuracy.

In our QD structures the wave function is strongly confined along the growth direction by the square well potential, so that we can approximate $(r^e_{\perp}-r^h_{\perp})^2$ in the Coulomb term with its average value l^2. We choose l to be twice the average length related to the ground state of an *infinite-height* square well of width *a*, i.e., $l=(2a/\pi)\sqrt{(\pi^2-6)/12}$. It is thus possible to separate the Hamiltonian (52) as $\mathbf{H}=\mathbf{H}_{\parallel}(\mathbf{r}_{e\parallel},\mathbf{r}_{h\parallel})+\mathbf{H}_{\perp}(r_{e\perp})+\mathbf{H}_{\perp}(r_{h\perp})$, where $\mathbf{H}_{\perp}(r_{i\perp})$

$=p_{r_{i\perp}}^2/2m_i+V_c^i(r_{i\perp})$ is the single-particle Hamiltonian along the growth direction—exactly solvable for the case of a parabolic potential as well as of an infinite-height square well. By further defining the center of mass (cm) and relative coordinates $\mathbf{R}=[m_e(\mathbf{r}_{e\|}-\mathbf{d}_\|^e)+m_h(\mathbf{r}_{h\|}-\mathbf{d}_\|^h)]/M$, $(M=m_e+m_h)$ and $\mathbf{r}=\mathbf{r}_{h\|}-\mathbf{r}_{e\|}$, the in-plane Hamiltonian $\mathbf{H}_\|$ becomes

$$\mathbf{H}_\|(\mathbf{R},\mathbf{r})=\frac{P^2}{2M}+\frac{1}{2}M\omega_R^2R^2+\frac{p}{2\mu}+\frac{1}{2}\mu\omega_r^2|\mathbf{d}-\mathbf{r}|^2$$

$$+\mu(\omega_e^2-\omega_h^2)\mathbf{R}\cdot(\mathbf{d}-\mathbf{r})-\frac{e^2}{\varepsilon_0\sqrt{r^2+l^2}}, \quad (54)$$

where $\mu=m_em_h/M$ is the reduced mass, $\omega_R^2=(1+\Delta)(\omega_e^2+\omega_h^2)/2$, $\omega_r^2=(1-\Delta)(\omega_e^2+\omega_h^2)/2$, $\Delta=[(m_e-m_h)/M](\omega_e^2-\omega_h^2)/(\omega_e^2+\omega_h^2)$, and

$$\mathbf{d}=-\mathbf{d}_\|^e+\mathbf{d}_\|^h=e\mathbf{F}\left(\frac{1}{m_e\omega_e^2}+\frac{1}{m_h\omega_h^2}\right) \quad (55)$$

denotes the total (electron+hole) field-induced in-plane displacement.

In the limit $(\omega_e^2-\omega_h^2)/(\omega_e^2+\omega_h^2)\ll 1$, the two coordinates are only weakly coupled, and the Schrödinger equation associated to the cm coordinate $\mathbf{R}$ is exactly solvable; in the general case, we shall concentrate on the ground state, though the generalization to higher states is straightforward. We can approximate the ground state of $\mathbf{H}_\|$ as $\Psi(\mathbf{r},\mathbf{R})=\Psi_x(x)\chi(y,\mathbf{R})$, where x and y denote, respectively, the components of $\mathbf{r}$ parallel and perpendicular to the field $\mathbf{F}$, $\chi(y,\mathbf{R})=e^{-y^2/2\lambda_r^2}/(\lambda_r^2\pi)^{1/4}\ e^{-R^2/2\lambda_R^2}/(\lambda_R^2\pi)^{1/2}$, $\lambda_r=\sqrt{\hbar/\mu\omega_r}$, and $\lambda_R=\sqrt{\hbar/M\omega_R}$. By averaging $\mathbf{H}_\|$ over $\chi(y,\mathbf{R})$, we get the effective Hamiltonian $\mathbf{H}_{\rm eff}=\frac{1}{2}\hbar\omega_r+\hbar\omega_R+p_x^2/2\mu+V_{\rm eff}(x)$, characterized by the effective potential

$$V_{\rm eff}(x)=\frac{1}{2}\mu\omega_r^2(x-d)^2+V_C\left(\frac{x^2+l^2}{2\lambda_r^2}\right). \quad (56)$$

with $V_C(u)=-(e^2/\varepsilon_0\sqrt{\pi}\lambda_r)e^uK_0(u)$, K_0 being the zero-order Bessel function.

Since $K_0(u)\overset{u\to\infty}{\sim}\sqrt{\pi/2u}e^{-u}$, in the limit $x\to\infty$, we regain the expected behavior for the Coulomb term

$$V_c\left(\frac{x^2+l^2}{2\lambda_r^2}\right)\overset{(x^2+l^2)/2\gg\lambda_r^2}{\sim}-\frac{e^2}{\varepsilon_0\sqrt{x^2+l^2}}\overset{|x|\gg l}{\approx}-\frac{e^2}{\varepsilon_0|x|}. \quad (57)$$

Notice that, considering the typical parameters of our systems ($l\approx 20$ Å and $\lambda_r\approx 50$ Å), according to Eq. (57) there exists a relevant range of values for x where we cannot approximate V_C by its simpler asymptotic, Coulomb-like form.

Since we are interested in the system ground state, we can approximate $V_{\rm eff}$ around its minimum

$$V_{\rm eff}(x)\approx V_0+\frac{1}{2}\mu\tilde{\omega}^2(x-x_0)^2, \quad (58)$$

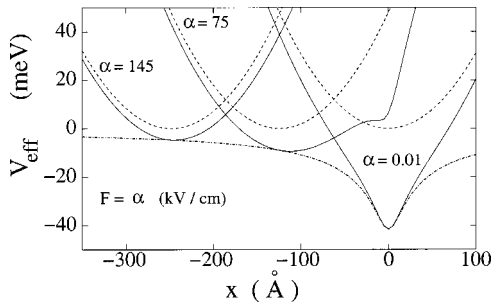

FIG. 12. Effective potential $V_{\rm eff}(x)$ (solid line) as a function of the x coordinate for three different values of the external field F. Here, the following parameters have been used: $m_e=0.067m_0$, $m_h=0.34m_0$, $\hbar\omega_e=30$ meV, $\hbar\omega_h=24$ meV. The dashed line represents the parabolic part of $V_{\rm eff}(x)$ and the dashed-dotted line the Coulomb term.

where $V_0\equiv V_{\rm eff}(x_0)$ and $\mu\bar{\omega}^2\equiv\partial^2V_{\rm eff}/\partial x^2|_{x_0}$. Within such approximation scheme, the eigenvalues and eigenfunctions of $\mathbf{H}_{\rm eff}$ can be evaluated analytically and, in particular, the approximate ground state eigenfunction becomes $\Psi_x(x)=(\mu\bar{\omega}/\hbar\pi)^{1/4}e^{-(1/2)(\mu\tilde{\omega}/\hbar)(x-x_0)^2}$. In the regime we are interested in (strong confinement and pronounced biexcitonic shift, i.e., large enough external field), the Coulomb attraction between electron and hole can be regarded as a perturbation. In this regime, its main effect is to reduce the displacement d between electron and hole wave-function centers to x_0, while the two single particle wave functions are, with a good approximation, rigidly translated. This can be understood by looking at Fig. 12, where the potential $V_{\rm eff}$ is plotted for three different values of the external field $\mathbf{F}$. The solid lines correspond to the full potential, the dashed lines to its parabolic part, the dashed-dotted line to the Coulomb part (independent of $\mathbf{F}$). For small and intermediate $\mathbf{F}$ the influence of the Coulomb field on the total potential is relevant. For intermediate fields the figure clearly shows that the minimum of the total potential is shifted with respect to the parabolic one. For strong and intermediate values of the applied field F, the effect of the shallow Coulomb potential on the region around the minimum of the total potential is mainly a rigid shift with respect to the unperturbed parabolic potential. For small fields, instead, the shape itself of the potential is definitely modified by the Coulomb term.

In the regime of interest, we can write x_0 as

$$x_0=d-\Delta x, \quad (59)$$

with $\Delta x\ll d$. By inserting Eq. (59) into $\partial V_{\rm eff}/\partial x|_{x_0}=0$ and considering, in the resulting equation, terms up to first order in Δx, the following analytical expression is obtained:

$$\frac{\Delta x}{d}=-\frac{\lambda_r}{a^{ex}}\frac{\exp(\xi)}{\sqrt{\pi}}\frac{\Delta K}{1-\dfrac{\lambda_r}{a^{\rm ex}}\dfrac{\exp(\xi)}{\sqrt{\pi}}\left[\dfrac{d^2}{\lambda_r^2}A(\Delta K,K_1)+\Delta K\right]}, \quad (60)$$

where $\xi=(d^2+l^2)/2\lambda_r^2$, K_1 denotes the first-order Bessel function, $\Delta K=K_0(\xi)-K_1(\xi)$, $A(\Delta K,K_1)=2\Delta K$

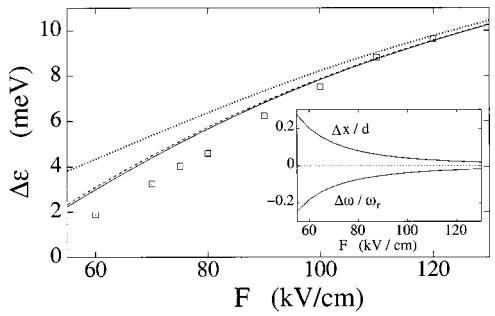

FIG. 13. Biexcitonic shift $\Delta\mathcal{E}$ as a function of the in-plane field F. Here, the parameters used are the same as in Fig. 12. The squares represent exact numerical results, the solid line the predictions of the model, the dashed line the predictions of the model after setting $\Delta\omega=0$, and the dotted line the results obtained by neglecting completely Coulomb interaction in the wave function. The inset reports the behavior of $\Delta\omega/\omega_r$ and $\Delta x/d$ for the same range of applied fields.

$+K_1(\xi)/\xi$, and a^{ex} is the excitonic Bohr radius introduced in Eq. (49). Notice that the prefactor $\lambda_r/a^{\mathrm{ex}}$ is a measure of the system confinement. In a similar way, setting $\tilde{\omega}=\omega_r+\Delta\omega$ in $\mu\tilde{\omega}=\partial^2 V_{\mathrm{eff}}/\partial x^2|_{x_0}$, we can calculate the effect of the Coulomb attraction on the potential shape

$$\frac{\Delta\omega}{\omega_r}=-\frac{\lambda_r}{a^{\mathrm{ex}}}\frac{\exp(\xi)}{2\sqrt{\pi}}\left(\frac{d^2}{\lambda_r^2}A(\Delta K,K_1)+\Delta K-\frac{\Delta x}{d}\frac{d^2}{\lambda_r^2}\left\{\frac{d^2}{\lambda_r^2}\left[2A(\Delta K,K_1)-\frac{1}{\xi}\left(\Delta K+2\frac{K_1(\xi)}{\xi}\right)\right]+3A(\Delta K,K_1)\right\}\right). \tag{61}$$

In the strong-field limit $\lambda_r^2/d^2\ll 1$ [see Eq. (55)], $\Delta\omega/\omega_r=-\Delta x/d\propto-(\lambda_r/a^{\mathrm{ex}})(\lambda_r^3/d^3)$, which shows that, in this regime, Coulomb corrections decrease very fast with increasing field. The condition $\Delta x/d\lesssim 20\%$ quantitatively defines the validity regime of the proposed approximation scheme. The latter coincides with the intermediate- and strong-field one, which is the regime of interest for the QD structures investigated below. It is also easy to show that in this regime the correction on the wave function due to $\Delta\omega/\omega_r$ is negligible with respect to the correction given by the shift $\Delta x/d$ (see also Fig. 13).

As previously discussed, the most important quantity for implementing our QIC scheme is the biexcitonic shift. This is in our case the energy shift due to the Coulomb interaction between two excitons sitting in neighboring dots (see Sec. III B). Within our model, we approximate the biexcitonic ground state as the product of two excitonic wave functions sitting in different dots and built according to the prescription given above. The wave function in the growth direction is approximated by a Gaussian of width $l/2$ and the two dots are taken to have the same width a, i.e., the average of the two dots widths. This is reasonable since, for construction, the two dots have almost the same width. The desired biexcitonic shift $\Delta\mathcal{E}$ is then obtained averaging the corresponding two-exciton Hamiltonian over such factorized ground state. Within this approximation scheme, $\Delta\mathcal{E}$ becomes an easy-to-calculate sum of at most 2D integrals. In the corresponding validity region the model provides a good estimate for $\Delta\mathcal{E}$: Fig. 13 shows a comparison between the exact results (diamonds), the approximate result (solid curve) and the results obtained by neglecting completely Coulomb correlation in the wave functions (dotted line). The dashed curve shows the approximated results obtained setting $\Delta\omega/\omega_r=0$: as anticipated before, this correction is generally negligible.

In order to implement our quantum computing scheme, system parameters as ω_e, ω_h, and $\mathbf{F}$ must satisfy some specific requirements. This determines the parameter space available in designing our QD structures. To this end, let us analyze the various constraints in details.

First of all, (i) in order to have well-defined qubits, tunneling between dots must be suppressed; in agreement with state-of-the-art nanostructure technology, we have chosen for our calculations barrier heights of 1 eV (electrons) and 0.58 eV (holes) and an interdot distance $D=100$ Å. On the other side, (ii) to implement our QIC scheme, Coulomb interaction between consecutive dots must be strong enough to produce a biexcitonic shift of the order of a few meV; this can be obtained either by tailoring in a suitable way the distance between the two dots or by varying the strength of the in-plane field $\mathbf{F}$, since as a rough approximation

$$\Delta\mathcal{E}\propto\frac{d^2}{D^3}, \tag{62}$$

where d is given by Eq. (55). Unfortunately, (iii) a side effect of a strong electric field $\mathbf{F}$ is to decrease the oscillator strength and, accordingly, the system response to driving laser pulses; indeed, the electric field induces a spatial separation between electron and hole wave functions, thus decreasing their overlap (see Fig. 4). If we now consider the confining parabolic potentials, (iv) in order to have well-defined quantum dots, the system must be in the strong-confinement regime previously introduced: the characteristic length λ_r associated to the parabolic potential in Eq. (54) must be smaller than the corresponding excitonic Bohr radius a^{ex}. On the other side, (v) as shown by Eq. (62) and Eq. (55), a too strong parabolic confinement would in turn heavily decrease the biexcitonic shift $\Delta\mathcal{E}$. Last but not least, (vi) in order to be able to perform general QIC schemes, we must be able to energetically address specific excitations of the system unambiguously. This means that the peaks of interest in the optical spectra, namely ground-state excitonic and biexcitonic states, must be well isolated from other high-energy transitions. This determines additional constraints on the value of $\hbar\omega_e$ and $\hbar\omega_h$.

From the above discussion, it is clear that in order to satisfy at the same time all the requirements listed above [(i)–(vi)], the system parameters must be fine tuned so that a quick mean to scan the whole parameter space becomes necessary. The simplified model previously described came out to be quite efficient in performing such detailed analysis. The available parameter space for a reasonable field of $F=75$ kV/cm is shown in Fig. 14. Here, the typical error in the

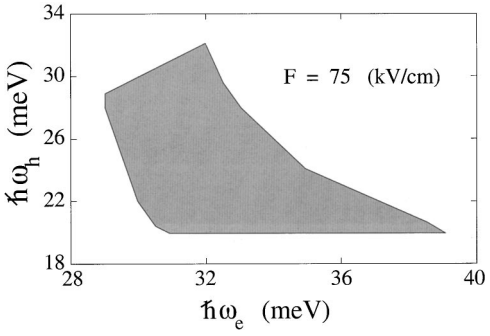

FIG. 14. Plot of the parameter space available for designing the QD molecule used as quantum hardware in our QIC implementation. This has been calculated using the proposed analytical model (see text).

calculated values of $\Delta\mathcal{E}$ is 10–20 %. The constraints imposed are $\Delta\mathcal{E}\geqslant 3.5$ meV, oscillator strength greater than $0.15\mu_{\rm bulk}$, $\hbar\omega_e > \hbar\omega_h$, $\hbar\omega_h - \Delta\mathcal{E}\geqslant 10$ meV, and $\lambda_r/d^{\rm ex}\leqslant 0.6$. Based on this analysis, we have identified the parameter set used in the simulated experiments of QIC processing presented in the following section.

IV. QUANTUM INFORMATION PROCESSING

As anticipated in the introductory part of the paper, the advent of QIC (Ref. 28) as an abstract concept, has stimulated a great deal of new thinking about how to design and realize quantum information processing devices. This goal is extremely challenging: generally speaking, one should be able to perform, on a system with a well-defined quantum state space (the *computational* space), precise quantum-state preparation, coherent quantum manipulations (*gating*) of arbitrary length, and state detection as well. It is well known that the major obstacle to implement this ideal scheme is *decoherence*: the spoiling of the unitary character of quantum evolution due to the uncontrollable coupling with environmental, i.e., noncomputational, degrees of freedom. Mostly due to the need of low decoherence rates, the first proposals for experimental realizations of quantum information processing devices originated from specialties in atomic physics,[29] in quantum optics,[30] and in nuclear and electron magnetic-resonance spectroscopy.[31] On the other hand, practically relevant quantum computations require a large number of quantum-hardware units (*qubits*), that are known to be hardly achievable in terms of such systems. In contrast, in spite of the serious difficulties related to the ''fast'' decoherence times, a solid-state implementation of QIC seems to be the only way to benefit synergically from the recent progress in ultrafast optoelectronics[32] as well as in meso/nanostructure fabrication and characterization.[4] Among the proposed solid-state implementations one should mention those in superconducting-device physics[33] and in meso- and nanoscopic physics.[34] In particular, the first semiconductor-based proposal, by Loss and DiVincenzo, relies on spin dynamics in quantum dots; it exploits the low decoherence of spin degrees of freedom in comparison to the one of charge excitations.

As originally envisioned in Ref. 14, gating of charge excitations could be performed by exploiting *present* ultrafast laser technology,[32] that allows one to generate and manipulate electron-hole quantum states on a subpicosecond time scale: *coherent-carrier-control*.[26] In this respect, decoherence times on nano/microsecond scales can be regarded as ''long'' ones. Based on this idea a few implementations have been recently put forward.[35] However, while in these proposals single-qubit operations are implemented by means of ultrafast optical spectroscopy, the control of two-qubit operations still involves the application of external fields and/or microcavity-mode couplings, whose switching times are much longer than decoherence times in semiconductors. It clearly follows that such proposals are currently out of reach in terms of state-of-the-art optoelectronics technology.

As already pointed out in Ref. 14, in order to take full advantage from modern ultrafast laser spectroscopy one should be able to design fully optical gating schemes able to perform single- *and* two-qubit operations on a subpicosecond time scale. Following this spirit, we have recently proposed the first *all-optical* implementation with semiconductor macromolecules.[15]

The aim of this section is to review and discuss the semiconductor-based implementation in Ref. 15, whose quantum hardware consists of coupled QD structures, similar to those investigated in Sec. III B. As described below, the crucial ingredient in our QIC scheme is the field-induced exciton-exciton coupling discussed in Sec. III. Indeed, the central idea in our QIC proposal is to exploit such few-exciton effects to design *conditional operations*.

A. Quantum hardware and computational subspace

As discussed in Sec. II E, two basic requirements are needed for QIC processing: (i) the tensor-product structure of the quantum hardware and (ii) the SU (2) character of the raising/lowering operators acting on the individual qubits. Based on the electro-optical-response analysis of Sec. III, we can conclude that state-of-the-art coupled QD structures can be used as semiconductor-based hardware for quantum information processing. Indeed, as shown in the previous section, these requirements are well fulfilled by the prototypical QD molecules studied above. Our detailed investigation has shown that a proper tailoring of the QD confinement potential as well as of the interdot distance allows one to identify a well-precise subset of excitonic states, corresponding to intradot ground-state excitons. Indeed, as clearly shown in Sec. III B (see Fig. 9), we can associate to each QD structure a ground-state exciton, i.e., its low-energy optical transition corresponding to the creation/destruction of a Coulomb-correlated electron-hole pair in that dot. We have shown that for these low-energy intradot optical transitions the corresponding exciton wavefunctions are localized in the various dots of the array; this allows us to label such subset of excitonic states according to their host QD. In addition, in view of the relatively strong carrier confinement, leakage effects (see Sec. II E) are expected to play a minor role.

More specifically, following the second-quantization notation, let us denote with $|n_\nu\rangle$ the absence ($n_\nu=0$—no conduction-band electrons—and the presence ($n_\nu=1$) of a

ground-state exciton—a Coulomb-correlated electron-hole pair—in dot ν; they constitute the single-qubit basis for the proposed QIC scheme $|0\rangle_\nu$ and $|1\rangle_\nu$. The whole computational state-space is then spanned by the basis set

$$|\{n_\nu\}\rangle = \otimes_\nu |n_\nu\rangle, \quad (n_\nu = 0,1). \tag{63}$$

The full many-body Hamiltonian $\mathbf{H} = \mathbf{H}^0 + \mathbf{H}'$ in Eq. (16) restricted to the above computational space will be described by the following matrix elements:

$$H_{\{n_\nu\}\{n'_\nu\}} = \langle\{n_\nu\}|(\mathbf{H}^0 + \mathbf{H}')|\{n'_\nu\}\rangle = H^0_{\{n_\nu\}\{n'_\nu\}} + H'_{\{n_\nu\}\{n'_\nu\}}. \tag{64}$$

They are the sum of two contributions: the first one is due to the Coulomb-correlated carrier-system Hamiltonian; the second is due to the carrier-light interaction Hamiltonian in Eq. (14). As discussed in Sec. II C, the latter describes the creation/destruction of electron-hole pairs driven by ultrafast sequences of multicolor laser pulses.

Let us now focus on the term H^0. As discussed in Sec. II B, it preserves the total number of electron-hole pairs N, and this is still true within our reduced—i.e., computational—subspace. In general, the Hamilton Matrix $H^0_{\{n_\nu\}\{n'_\nu\}}$ is nondiagonal. However, for the case of the realistic coupled QD structure analyzed in Sec. III B, nondiagonal terms are found to play a very minor role. In this case, the latter can be neglected and the Hamiltonian matrix H^0 is then diagonal in our number representation $\{n_\nu\}$. This suggests to introduce corresponding number operators acting on our computational subspace: $\mathbf{n}_\nu = \Sigma^1_{n_\nu=0} |n_\nu\rangle n_\nu \langle n_\nu| = |1\rangle_\nu \langle 1|_\nu$. The Hamiltonian $\mathbf{H}^0$ reduced to our computational subspace can then be expressed in terms of such number operators. In particular, for an array of coupled QD's this can be written as

$$\tilde{\mathbf{H}}^0 = \sum_\nu \mathcal{E}_\nu \mathbf{n}_\nu + \frac{1}{2}\sum_{\nu\nu'} \Delta\mathcal{E}_{\nu\nu'} \mathbf{n}_\nu \mathbf{n}_{\nu'}. \tag{65}$$

Here, $\mathcal{E}_\nu$ denotes the energy of the ground-state exciton in dot ν while $\Delta\mathcal{E}_{\nu\nu'}$ is the biexcitonic shift due to the Coulomb interaction between dots ν and ν', introduced in Sec. III [see Eq. (50) and Fig. 11].

The effective Hamiltonian in Eq. (65) has exactly the same structure of the one proposed by Lloyd in his pioneering paper on quantum cellular automata,[36] and it is the Model Hamiltonian currently used in most of the NMR quantum-computing schemes.[37] This fact is extremely important since it tells us the following.

(i) The present semiconductor-based implementation contains all relevant ingredients for the realization of basic QIC processing.

(ii) It allows one to establish a one-to-one correspondence between our semiconductor-based scheme and much more mature implementations, such as NMR.[37]

According to Eq. (65), the single-exciton energy $\mathcal{E}_\nu$ is renormalized by the biexcitonic shift $\Delta\mathcal{E}_{\nu\nu'}$, induced by the presence of a second exciton in dot ν':

$$\tilde{\mathcal{E}}_\nu = \mathcal{E}_\nu + \sum_{\nu'\neq\nu} \Delta\mathcal{E}_{\nu\nu'} n_{\nu'}. \tag{66}$$

In order to better illustrate this idea, let us focus again on the two-QD structure, i.e., two-qubit system, of Fig. 9 and fix our attention on one of the two dots, say dot b. The effective energy gap between $|0\rangle_b$ and $|1\rangle_b$ depends now on the occupation of dot a. This elementary remark suggests that we design properly tailored laser-pulse sequences to implement conditional logic gates between the two QD qubits as well as single-qubit rotations. Indeed, by sending an ultrafast laser π-pulse with central energy $\hbar\omega_b[n_a] = \mathcal{E}_b + \Delta\mathcal{E}_{ba} n_a$, the transition $|n_b\rangle \rightarrow |1-n_b\rangle$ (π rotation) of the target qubit (dot b) is obtained if and only if the control qubit (dot a) is in the state $|n_a\rangle$. Notice that the above scheme corresponds to the so-called selective population transfer in NMR;[37] alternative procedures used in that field can be adapted to the present proposal as well. Moreover, by denoting with $\mathcal{U}_b^{n_a}$ the generic unitary transformation induced by the laser π pulse of central frequency $\omega_b[n_a]$, it is easy to check that the two-color pulse sequence $\mathcal{U}_b^0 \mathcal{U}_b^1$ achieves the unconditional π rotation of qubit b.

B. A few simulated experiments

In order to test the viability of the proposed quantum-computation strategy, we have performed a few simulated experiments of basic quantum information processing. To this aim, we have performed a direct time-dependent solution of the generalized Liouville-von Neumann equation in Eq. (31) restricted to our computational subspace, i.e., we have simulated the time evolution of the reduced density matrix

$$\rho_{\{n_\nu\}\{n'_\nu\}}(t) = \langle\{n_\nu\}|\rho(t)|\{n'_\nu\}\rangle. \tag{67}$$

As discussed in Sec. II D, this is governed by the total Hamiltonian $\mathcal{H}$ reduced to our computational subspace [see Eqs. (64) and (65)] plus a nonunitary term[23] due to energy-relaxation and dephasing processes induced by environmental degrees of freedom, such as phonons, plasmons, etc. The latter has been treated within the standard T_1T_2 model.[38]

We stress that the present density-matrix description, restricted to our computational subspace, does not account for *leakage effects*, i.e., it neglects processes connecting states of the computational subspace to other—noncomputational—excitonic states, and vice versa. Due to the strong-confinement character of our QD structures (see Sec. III) such leakage effects are expected to play a very minor role. A quantitative evaluation of the leakage dynamics would require the inclusion in our density-matrix description of noncomputational states.

The above simulation scheme has been applied to the coupled-QD structure of Fig. 9 in the presence of an in-plane static field $F = 75$ kV/cm: $\mathcal{E}_a = 1.673$ eV, $\mathcal{E}_b = 1.683$ eV, and $\Delta\mathcal{E} = 4$ meV (see inset in Fig. 10).

We shall start our time-dependent analysis by simulating a basic conditional two-qubit operation, the so-called *controlled not* (CNOT) gate. Our first simulated experiment is shown in Fig. 15. The multicolor laser-pulse train (see cen-

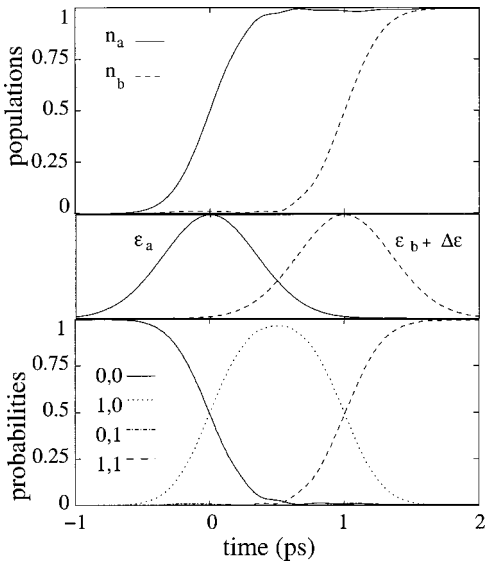

FIG. 15. Time-dependent simulation of a two-qubit operation realizing the first prescription ($|1,0\rangle \rightarrow |1,1\rangle$) for a CNOT logic quantum gate on dots a and b (see text). Exciton populations n_a and n_b (upper panel) and diagonal density-matrix elements (lower panel) as a function of time. The laser-pulse sequence is also sketched (central panel).

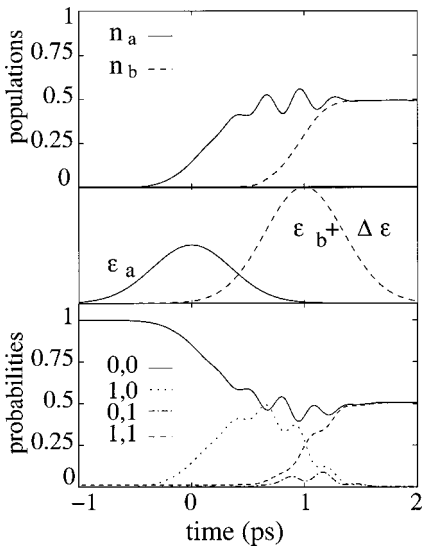

FIG. 16. Time-dependent simulation of a CNOT quantum gate transforming the factorized state $|0,0\rangle + |1,0\rangle$ into a maximally entangled state $|0,0\rangle + |1,1\rangle$ for the coupled QD structure $a+b$ in Fig. 9 (see text). Exciton populations n_a and n_b (upper panel) and diagonal density-matrix elements (lower panel) as a function of time. The laser-pulse sequence is also sketched (central panel).

tral panel) is able to perform first a π rotation of the qubit a; Then, the second pulse is tuned to the frequency $\mathcal{E}_b + \Delta\mathcal{E}$, thus performing a π rotation of the qubit b since this corresponds to its renormalized transition energy [see Eq. (66)] when the neighbor qubit a is in state $|1\rangle_a$. The scenario described so far is confirmed by the time evolution of the exciton occupation numbers n_a and n_b (upper panel) as well as of the diagonal elements of the density matrix in our four-dimensional computational basis (lower panel).

More specifically, at the beginning the system is in the state $|0,0\rangle \equiv |0\rangle_a \otimes |0\rangle_b$. Due to the first pulse at $t=0$ the computational state moves to the state $|1,0\rangle \equiv |1\rangle_a \otimes |0\rangle_b$. Finally, at time $t=1$ ps the second pulse brings the system into the state $|1,1\rangle \equiv |1\rangle_a \otimes |1\rangle_b$.

This realizes the first part of the well-known CNOT gate: the target qubit b is rotated if the control qubit a is in state $|1\rangle_a$. To complete it, one has to show that the state of the target qubit b remains unchanged if the control qubit a is in state $|0\rangle_a$. This has been checked by a second simulated experiment (not reported here) where the first pulse, being now off-resonant (with respect to dot a), does not change the computational state of the system. As a consequence, the second pulse is no more into resonance with the excitonic-transition energy of dot b, since the latter is no more renormalized by the excitonic occupation of dot a. Therefore, the initial state of the system is $|0,0\rangle$ and the final one is again $|0,0\rangle$.

The simulated experiments discussed so far clearly show the potential realization of the CNOT gate, thus confirming the validity of the proposed semiconductor-based QIC strategy. However, the analysis presented so far deals with factorized states, i.e., we have simulated the CNOT gate acting on basis states $|\{n_\nu\}\rangle$ only. It is well known[28] that the key ingredient in any quantum-computation protocol is entanglement. Generally speaking, this corresponds to a nontrivial linear combination of our basis states.

We shall now show that the CNOT gate previously discussed is able to transform a factorized state into a maximally entangled one. Figure 16 shows a simulated two-qubit operation driven again by a two-color laser-pulse sequence (see central panel). Initially, the system is in the state $|0,0\rangle$. The first laser pulse (at $t=0$) is tailored in such a way to induce now a $\pi/2$ rotation of the qubit a: $|0,0\rangle \rightarrow (|0,0\rangle + |1,0\rangle)/\sqrt{2}$. At time $t=1$ ps a second pulse induces a conditional π rotation of the qubit b: $|0,0\rangle + |1,0\rangle \rightarrow |0,0\rangle + |1,1\rangle$. This last operation plays a central role in any QIC processing, since it transforms a *factorized* state $[(|0\rangle_a + |1\rangle_a) \otimes |0\rangle_b]$ into an *entangled* state $(|0\rangle_a \otimes |0\rangle_b + |1\rangle_a \otimes |1\rangle_b)$.

As we can see, during the pulse energy-nonconserving (or off-resonant) transitions[2] take place; however, at the end of the pulse such effects vanish and the desired quantum state is reached. The experiments simulated above (see Figs. 15 and 16) clearly show that the energy scale of the biexcitonic splitting $\Delta\mathcal{E}$ in our QD molecule (see Fig. 11) is compatible with the subpicosecond operation time scale of modern ultrafast laser technology.[32]

V. SUMMARY AND CONCLUSIONS

We have presented a detailed analysis of the electro-optical response of single as well as coupled QD structures. More specifically, we have investigated the effect of a static electric field on the many-exciton optical response of quasi-0D semiconductor nanostructures. Our analysis has shown that a proper tailoring of the single-particle confinement potential as well as of the interdot distance and applied

field allows one to induce and control intradot as well as interdot exciton-exciton coupling; this, in turn, may give rise to significant energy shifts of the optical transitions.

This field-induced dipole-dipole coupling constitutes the key ingredient of the proposed all optical implementation of QIC with a semiconductor-based quantum hardware. Our analysis has shown that energy-selected optical transitions in realistic state-of-the-art QD structures are good candidates for quantum-information encoding and manipulation. The subpicosecond time scale of ultrafast laser spectroscopy allows for a relatively large number of elementary operations within the exciton decoherence time.

At this point a few comments are in order. First, we stress a very important feature of the proposed semiconductor-based implementation: as for NMR quantum computing, two-body interactions are always switched on (this should be compared to the schemes in which two-qubit gates are realized by turning on and off the coupling between subsystems, e.g., by means of slowly varying fields and cavity-mode couplings); conditional as well as unconditional dynamics is realized by means of sequences of ultrafast single-qubit operations whose length does not scale as a function of the total number of QD's in the array.[39]

Let us now come to the *state measurement*. In view of the few-exciton character of the proposed quantum hardware, the conventional measurement of the carrier subsystem by spectrally resolved luminescence needs to be replaced by more sensitive detection schemes. To this end, a viable strategy could be to apply to our semiconductor-based structure the well-known recycling techniques commonly used in quantum-optics experiments.[40] Generally speaking, the idea is to properly combine quantum- and dielectric-confinement effects in order to obtain well-defined energy levels, on which design energy-selective photon-amplification schemes. An alternative approach would be to adopt a *storage-qubit scheme*, as recently proposed in Ref. 41.

The nanoscale range of the interdot coupling we employed for enabling conditional dynamics does not allow for space-selective optical addressing of individual qubits. For this reason, at least for our basic QD molecule $(a+b)$, we resorted to an energy-selective addressing scheme. However, extending such strategy to the whole QD array would imply different values of the excitonic transition in each QD, i.e., $\mathcal{E}_\nu \neq \mathcal{E}_{\nu'}$. This, besides obvious technological difficulties, would constitute a conceptual limitation of scalability towards massive quantum computations. The problem can be avoided following a completely different strategy originally proposed by Lloyd[36] and recently improved in Ref. 42: by properly designed sequences of multicolor global pulses within a cellular-automaton scheme, local addressing is replaced by information-encoding transfer along our QD array.

Finally, a present limitation of the proposed quantum hardware are the nonuniform structural and geometrical properties of the QD's in the array, which may give rise to energy broadenings larger than the biexcitonic shift. However, recent progress in QD fabrication—including the realization of QD structures in microcavities—will allow us, we believe, to overcome this purely technological limitation.

ACKNOWLEDGMENTS

We are grateful to David DiVincenzo, Rita Iotti, Neil Johnson, Seth Lloyd, Ehoud Pazy, and Peter Zoller for stimulating and fruitful discussions. This work has been supported in part by the European Commission through the Research Project *SQID* within the *Future and Emerging Technologies (FET)* program.

APPENDIX A: EVALUATION OF SINGLE-PARTICLE PROPERTIES

In this section we shall describe the numerical approach used for the evaluation of the single-particle properties—3D wave functions and energy levels—for single as well as coupled QD structures. Within the standard envelope-function picture,[19] the noninteracting carriers in our quasi-0D structure in the presence of a static electric field are described by the Schrödinger equation (1) with the confinement potential in Eq. (42):

$$\left[-\frac{\hbar^2\nabla_{\mathbf{r}}^2}{2m_{e/h}}+V_c^{e/h}(\mathbf{r})\pm e\mathbf{F}\cdot\mathbf{r}\right]\psi_{i/j}(\mathbf{r})=\epsilon_{i/j}\psi_{i/j}(\mathbf{r}). \quad \text{(A1)}$$

As for the case of semiconductor quantum wires,[24] a quantitative analysis of the whole single-particle spectrum $\epsilon_{i/j}$ requires a direct numerical solution of the above Schrödinger equation. This can be performed using a fully 3D plane-wave expansion described in Ref. 25, which is a straightforward generalization to QD structures of the 2D plane-wave expansion proposed in Ref. 24.

As anticipated in Sec. III, when—as in this paper—we are interested in the low-energy range only, for most of the QD structures realized so far the carrier confinement can be described as the sum of two potential profiles acting along different directions [see Eq. (43)], which allows us to factorize the original 3D problem in Eq. (A1) into a perpendicular ($\perp$) direction and a parallel ($\parallel$) plane [see Eqs. (44) and (45)]. Moreover, as far as the low-energy region is concerned, the in-plane or parallel confinement is well described by a 2D parabolic potential. In this case the Schrödinger equation within the 2D parallel subspace can be solved analytically (see below) and thus our problem reduces to a numerical solution of the Schrödinger equation along the perpendicular direction

$$\mathcal{H}\psi^{\perp}_{i_\perp/j_\perp}(r_\perp)=-\left[-\frac{\hbar^2\nabla^2_{r_\perp}}{2m_{e/h}}+V_\perp^{e/h}(r_\perp)\pm eF_\perp r_\perp\right]\psi^{\perp}_{i_\perp/j_\perp}(r_\perp)$$
$$=\epsilon^{\perp}_{i_\perp/j_\perp}\psi^{\perp}_{i_\perp/j_\perp}(r_\perp). \quad \text{(A2)}$$

This has been solved using the plane-wave-expansion technique previously discussed.[24,25] Within such approach, the unknown envelope function is written as a linear combination of plane waves, i.e.,

$$\psi^{\perp}_{i_\perp/j_\perp}(r_\perp)=\frac{1}{\sqrt{L}}\sum_G b_G e^{iGr_\perp}, \quad \text{(A3)}$$

where $G=n(2\pi/L)$ are reciprocal lattice vectors associated to the periodicity box L. By substituting the above plane-wave expansion into Eq. (A2), the latter is transformed into the following eigenvalue problem:

$$\sum_G (\mathcal{H}_{GG'}-\epsilon^{\perp}\delta_{GG'})b_{G'}=0, \tag{A4}$$

where $\mathcal{H}_{GG'}$ are the matrix elements of the single-particle Hamiltonian in Eq. (A2) within our plane-wave basis. A direct diagonalization of $\mathcal{H}_{GG'}$ will then provide the desired perpendicular energy levels $\epsilon^{\perp}$ as well as the wavefunction coefficients b_G.

Let us now come back to the in-plane or parallel-subspace problem, which we treat within the 2D parabolic-confinement model previously mentioned, i.e.,

$$V_{\parallel}^{e/h}(\mathbf{r}_{\parallel})=\frac{1}{2}k_{e/h}r_{\parallel}^2. \tag{A5}$$

The corresponding Schrödinger equation is of the form

$$\left[-\frac{\hbar^2\nabla_{\mathbf{r}_{\parallel}}^2}{2m_{e/h}}+\frac{1}{2}k_{e/h}r_{\parallel}^2\pm e\mathbf{F}_{\parallel}\cdot\mathbf{r}_{\parallel}\right]\psi_{i_{\parallel}/j_{\parallel}}^{\parallel}(\mathbf{r}_{\parallel})=\epsilon_{i_{\parallel}/j_{\parallel}}^{\parallel}\psi_{i_{\parallel}/j_{\parallel}}^{\parallel}(\mathbf{r}_{\parallel}). \tag{A6}$$

It is well known that the presence of a static uniform electric field $\mathbf{F}_{\parallel}$ does not change the parabolic nature of our confinement potential. Indeed, Eq. (A6) can be rewritten as

$$\left[-\frac{\hbar^2\nabla_{\mathbf{r}_{\parallel}}^2}{2m_{e/h}}+\frac{1}{2}k_{e/h}|\mathbf{r}_{\parallel}-\mathbf{d}_{\parallel}^{e/h}|^2\right]\psi_{i_{\parallel}/j_{\parallel}}^{\parallel}(\mathbf{r}_{\parallel})=(\epsilon_{i_{\parallel}/j_{\parallel}}^{\parallel}-\Delta\epsilon_{e/h})\psi_{i_{\parallel}/j_{\parallel}}^{\parallel}(\mathbf{r}_{\parallel}). \tag{A7}$$

The presence of the applied field results in a shift

$$\mathbf{d}_{\parallel}^{e/h}=\mp\frac{e\mathbf{F}_{\parallel}}{k_{e/h}} \tag{A8}$$

of the parabolic-potential minimum as well as in a rigid energy shift

$$\Delta\epsilon_{e/h}=-\frac{1}{2}k_{e/h}\mathbf{d}_{\parallel}^{e/h^2}, \tag{A9}$$

often referred to as Stark shift. We stress that in the presence of the electric field $\mathbf{F}_{\parallel}$ we have different symmetry centers for electrons and holes; this, in turn, introduces significant modifications in the selection rules governing interband optical transitions (see below).

As anticipated, the Schrödinger equation (A7) can be solved analytically. Due to the central symmetry of the problem (with respect to the parabolic-potential minimum $\mathbf{d}_{\parallel}^{e/h}$), it is convenient to adopt a 2D polar-coordinate set. By denoting with $r=|\mathbf{r}_{\parallel}-\mathbf{d}_{\parallel}^{e/h}|$ the radial coordinate and with φ the azimuthal coordinate measured with respect to the field direction, we have

$$\psi_{nm}^{\parallel}(r,\varphi)=\alpha^{-(|m|+1)}\sqrt{\frac{n!}{\pi(n+|m|)!}}\times e^{-im\varphi}r^{|m|}e^{-r^2/2\alpha^2}\mathcal{L}_n^{|m|}\left(\frac{r^2}{\alpha^2}\right), \tag{A10}$$

where

$$\alpha=\left(\frac{m_{e/h}\omega_{e/h}}{\hbar}\right)^{-1/2} \tag{A11}$$

is the spatial extension of the harmonic-oscillator ground state—$\omega_{e/h}=\sqrt{k_{e/K}/m_{e/h}}$ being its oscillation frequency—while $\mathcal{L}_n^{|m|}(x)$ denotes the generalized Laguerre polynomial in the dimensionless variable $x=r^2/\alpha^2$.

In view of the central symmetry of the problem, our quantum numbers are those of the angular momentum in two dimensions, i.e., a radial number n ($n=0,1,2,...$) plus an orbital number m ($m=-n,-n+2,...,n-2,n$). The corresponding in-plane single-particle energy spectrum is given by

$$\epsilon_{nm}^{\parallel}=\hbar\omega_{e/h}(2n-|m|+1)=\hbar\omega_{e/h}(n_{\epsilon}+1), \tag{A12}$$

where $n_{\epsilon}=2n-|m|$ denotes the energy quantum number with degeneracy $(n_{\epsilon}+1)$.

The 3D single-particle energy spectrum is then given by the sum of equally-spaced energy-level sequences, i.e.,

$$\epsilon_l=\epsilon_{l_{\perp}}^{\perp}+\epsilon_{nm}^{\parallel}=\epsilon_{l_{\perp}}^{\perp}+(n_{\epsilon}+1)\hbar\omega_{e/h}: \tag{A13}$$

for each energy level $\epsilon^{\perp}$—obtained by solving the eigenvalue problem in (A4)—we deal with an harmonic-oscillator spectrum with energy separation $\hbar\omega_{e/h}$.

Given the single-particle state factorization in Eq. (44), the corresponding dipole matrix elements in Eq. (15) can be factorized as well

$$\mu_{ij}=\mu_{bulk}\mathcal{I}_{i_{\perp}j_{\perp}}^{\perp}\mathcal{I}_{i_{\parallel}j_{\parallel}}^{\parallel}, \tag{A14}$$

with

$$\mathcal{I}_{i_{\perp}j_{\perp}}^{\perp}=\int\psi_{i_{\perp}}^{\perp}(r_{\perp})\psi_{j_{\perp}}^{\perp}(r_{\perp})dr_{\perp} \tag{A15}$$

and

$$\mathcal{I}_{i_{\parallel}j_{\parallel}}^{\parallel}=\int\psi_{i_{\parallel}}^{\parallel}(\mathbf{r}_{\parallel})\psi_{j_{\parallel}}^{\parallel}(\mathbf{r}_{\parallel})d\mathbf{r}_{\parallel}. \tag{A16}$$

By inserting the plane-wave expansion (A3) into Eq. (A15), we get

$$\mathcal{I}_{i_{\perp}j_{\perp}}^{\perp}=\sum_G b_G^{i_{\perp}}b_G^{j_{\perp}}. \tag{A17}$$

Let us finally focus on the in-plane integral in Eq. (A16). This can be rewritten in terms of the polar-coordinate set r, φ introduced in Eq. (A10):

$$\mathcal{I}_{nm,n'm'}^{\parallel}=\int\psi_{nm}^{\parallel}(r_e,\varphi_e)\psi_{n'm'}^{\parallel}(r_h,\varphi_h)d\mathbf{r}_{\parallel}. \tag{A18}$$

Here, $r_{e/h}=|\mathbf{r}_\parallel-\mathbf{d}_\parallel^{e/h}|$ and $\varphi_{e/h}$ are the corresponding azimuthal angles. In general, the two polar-coordinate sets for electrons and holes do not coincide. Indeed, in the presence of a static field $F_\parallel$ we have different symmetry centers [see Eq. (A8)]. In contrast, for $F_\parallel=0$ the two coordinate sets coincide ($\mathbf{r}_\parallel\equiv r,\varphi=r_e,\varphi_e=r_h,\varphi_h$) and the above equation reduces to

$$\mathcal{I}^\parallel_{nm,n'm'}=\int \psi^\parallel_{nm}(r,\varphi)\psi^\parallel_{n'm'}(r,\varphi)rdrd\varphi. \quad \text{(A19)}$$

In this case—for which the symmetry centers for electrons and holes coincide—we deal with a number of well-known selection rules. In particular we have

$$\mathcal{I}^\parallel_{nm,n'm'}\propto\delta_{m+m'}. \quad \text{(A20)}$$

This tells us that in the electron-hole generation process the total angular momentum is conserved. Moreover, for the special case of equally extended electron and hole wave functions, i.e., $\alpha_e=\alpha_h$ (see discussion in Sec. III A), we have

$$\mathcal{I}^\parallel_{nm,n'm'}\propto\delta_{m+m'}\delta_{n,n'}=\delta_{m+m'}\delta_{n_e,n'_e}, \quad \text{(A21)}$$

i.e., the energy quantum number n_ϵ is conserved as well.

In contrast, in the presence of the static field the above selection rules are violated, due to the fact that the Harmonic-oscillator wave functions in Eq. (A10) are no longer eigenstates of the total angular momentum. As we shall see, the same considerations apply to the case of the two-body Coulomb matrix elements discussed in the following section.

APPENDIX B: EVALUATION OF TWO-BODY COULOMB MATRIX ELEMENTS

In this section we shall describe the numerical approach used for the evaluation of the two-body Coulomb matrix elements. Starting again from the single-particle state factorization in Eq. (44), the Coulomb matrix elements in Eq. (5) can be rewritten as

$$V_{l'_1l'_2l_2l_1}=\int d\mathbf{r}_\parallel\int d\mathbf{r}'_\parallel\,\psi^{\parallel *}_{n'_1m'_1}(\mathbf{r}_\parallel)\psi^{\parallel *}_{n'_2m'_2}(\mathbf{r}'_\parallel)V^\parallel_{l'_1l'_2l_2l_1}(\mathbf{r}_\parallel-\mathbf{r}'_\parallel)\times\psi^\parallel_{n_2m_2}(\mathbf{r}'_\parallel)\psi^\parallel_{n_1m_1}(\mathbf{r}_\parallel), \quad \text{(B1)}$$

where

$$V^\parallel_{l'_1l'_2l_2l_1}(\mathbf{r}_\parallel-\mathbf{r}'_\parallel)=\int d\mathbf{r}_\perp\int d\mathbf{r}'_\perp\,\psi^{\perp *}_{l'_1}(r_\perp)\psi^{\perp *}_{l'_2}(r'_\perp)\times V(\mathbf{r}-\mathbf{r}')\psi^\perp_{l_2}(r'_\perp)\psi^\perp_{l_1}(r_\perp) \quad \text{(B2)}$$

can be regarded as an in-plane effective potential obtained by integrating the original 3D Coulomb potential V—multiplied by the corresponding wave functions $\psi^\perp$—over the perpendicular direction.

Let us consider the explicit form of the 3D Coulomb potential in Eq. (B2) written in terms of its Fourier transform along the perpendicular direction

$$V(\mathbf{r}-\mathbf{r}')=\frac{e^2}{\varepsilon_0|\mathbf{r}-\mathbf{r}'|}=\frac{e^2}{\varepsilon_0\pi}\int dqK_0(q|\mathbf{r}_\parallel-\mathbf{r}'_\parallel|)e^{iq(r_\perp-r'_\perp)}. \quad \text{(B3)}$$

Here, ε_0 is the static dielectric constant,[43] q denotes the Fourier-transform parameter, while

$$K_0(x)=\int_0^\infty\frac{\cos y\,dy}{\sqrt{x^2+y^2}} \quad \text{(B4)}$$

is the zero-order modified Bessel function.

By inserting the Fourier expansion (B3) into Eq. (B2), we realize a factorization of the two space coordinates $r_\perp$ and $r'_\perp$. Indeed, by introducing the form factors

$$\mathcal{F}_{ll'}(q)=\int dr_\perp\psi^{\perp *}_l(r_\perp)e^{iqr_\perp}\psi^\perp_{l'}(r_\perp), \quad \text{(B5)}$$

the Coulomb matrix elements in Eq. (B2) can be simply written as

$$V^\parallel_{l'_1l'_2l_2l_1}(\mathbf{r}_\parallel-\mathbf{r}'_\parallel)=\frac{e^2}{\varepsilon_0\pi}\int K_0(q|\mathbf{r}_\parallel-\mathbf{r}'_\parallel|)\mathcal{F}_{l'_1l_1}(q)\mathcal{F}^*_{l'_2l_2}(q)dq. \quad \text{(B6)}$$

Therefore, the evaluation of the effective Coulomb potential in Eq. (B2) reduces to the evaluation of the form factors $\mathcal{F}$ in Eq. (B5). To this end, by replacing the wave functions $\psi^\perp$ with their plane-wave expansion in Eq. (A3) we get

$$\mathcal{F}_{ll'}(q)=\sum_{GG'}b^{l*}_Gb^{l'}_{G'}O(G'-G+q), \quad \text{(B7)}$$

where

$$O(k)=\frac{1}{L}\int e^{ikr_\perp}dr_\perp \quad \text{(B8)}$$

are plane-wave overlap integrals over the periodicity region L, whose explicit form can be evaluated analytically.

Therefore, for any shape of the perpendicular confinement potential, starting from the numerically computed eigenvectors b_G [see Eqs. (A3) and (A4)], we are able to obtain the various form factors $\mathcal{F}$ which, in turn, allow us to numerically evaluate the effective in-plane Coulomb potential in Eq. (B2). Once the latter is known over a suitable space grid, the original six-dimensional integral in Eq. (5) is then reduced to the evaluation of the four-dimensional integral in Eq. (B1). This requires some care, since the effective potential $V^\parallel$ is singular for $|\mathbf{r}_\parallel-\mathbf{r}'_\parallel|=0$. In order to eliminate such singularity, it is convenient to replace the integration coordinate $\mathbf{r}'_\parallel$ with the relative coordinate $\overline{\mathbf{r}}_\parallel=\mathbf{r}_\parallel-\mathbf{r}'_\parallel$. Indeed, if we move to 2D polar-coordinate sets for the new integration variables $\mathbf{r}_\parallel$ and $\overline{\mathbf{r}}_\parallel$, the presence of the Jacobian function corresponding to the relative coordinate $\overline{\mathbf{r}}_\parallel$ cancels the potential singularity.

We stress that—as for the case of optical matrix elements previously discussed (see Appendix A)—in the absence of applied static fields the symmetry centers for electrons and holes coincide [see Eq. (A8)] and, due to global rotation symmetry, we get

$$V_{l_1' l_2' l_2 l_1} \propto \delta_{m_1+m_2, m_1'+m_2'} \tag{B9}$$

and the numerical integration in Eq. (B1) reduces to three variables only: one angular and two radial coordinates. As for the optical matrix elements previously discussed, the selection rule in Eq. (B9) describes the conservation of the total angular momentum in the Coulomb interaction process: $m_1+m_2=m_1'+m_2'$.

In contrast, in the presence of an applied static field the selection rule (B9) is relaxed and we need to numerically solve the four-dimensional integral in Eq. (B1).

APPENDIX C: EVALUATION OF MANY-EXCITON STATES AND OPTICAL MATRIX ELEMENTS

In this section we shall apply the exact-diagonalization approach introduced in Sec. II B to the excitonic ($N=1$) and biexcitonic ($N=2$) case. Generally speaking, the method consists in a numerical diagonalization of the interacting-carrier Hamiltonian $\mathbf{H}^\circ$ written in the single-particle basis $\{|l_N\rangle\}$ [see Eqs. (8), (11), and (12)].

For the evaluation of excitonic states, i.e., states corresponding to a single Coulomb-correlated electron-hole pair, the proper basis set is given by the single-particle states in Eq. (10) with $N=1$, i.e.,

$$|l_1\rangle \equiv |i_1 j_1\rangle = c_{i_1}^\dagger d_{j_1}^\dagger |0\rangle. \tag{C1}$$

The corresponding Hamiltonian matrix is given by

$$H^\circ_{i_1 j_1, i_1' j_1'} = H^c_{i_1 j_1, i_1' j_1'} + H^{cc}_{i_1 j_1, i_1' j_1'} \tag{C2}$$

with

$$H^c_{i_1 j_1, i_1' j_1'} = \langle i_1 j_1 | \mathbf{H}^c | i_1' j_1' \rangle \tag{C3}$$

and

$$H^{cc}_{i_1 j_1, i_1' j_1'} = \langle i_1 j_1 | \mathbf{H}^{cc} | i_1' j_1' \rangle. \tag{C4}$$

Combining Eq. (C1) with the explicit form of the noninteracting Hamiltonian $\mathbf{H}^c$ in Eq. (3) and making use of the Fermionic commutation relations we get

$$H^c_{i_1 j_1, i_1' j_1'} = (\epsilon_{i_1} + \epsilon_{j_1}) \delta_{i_1 j_1, i_1' j_1'}. \tag{C5}$$

In a similar way, combining Eq. (C1) with the explicit form of the carrier-carrier Hamiltonian $\mathbf{H}^{cc}$ in Eq. (4), after a straightforward calculation we obtain $H^{cc}_{i_1 j_1, i_1' j_1'} = -V_{i_1 j_1 j_1' i_1'}$.

Let us now come to the evaluation of biexcitonic states, i.e., states corresponding to two Coulomb-correlated electron-hole pairs. In this case the proper basis set is given by the single-particle states in Eq. (10) with $N=2$, i.e.,

$$|l_2\rangle \equiv |i_1 j_1 i_2 j_2\rangle = c_{i_1}^\dagger d_{j_1}^\dagger c_{i_2}^\dagger d_{j_2}^\dagger |0\rangle. \tag{C6}$$

The corresponding Hamiltonian matrix is given by

$$H^\circ_{i_1 j_1 i_2 j_2, i_1' j_1' i_2' j_2'} = H^c_{i_1 j_1 i_2 j_2, i_1' j_1' i_2' j_2'} + H^{cc}_{i_1 j_1 i_2 j_2, i_1' j_1' i_2' j_2'} \tag{C7}$$

with

$$H^c_{i_1 j_1 i_2 j_2, i_1' j_1' i_2' j_2'} = \langle i_1 j_1 i_2 j_2 | \mathbf{H}^c | i_1' j_1' i_2' j_2' \rangle \tag{C8}$$

and

$$H^{cc}_{i_1 j_1 i_2 j_2, i_1' j_1' i_2' j_2'} = \langle i_1 j_1 i_2 j_2 | \mathbf{H}^{cc} | i_1' j_1' i_2' j_2' \rangle. \tag{C9}$$

Again, combining Eq. (C6) with the explicit form of the noninteracting Hamiltonian $\mathbf{H}^c$ in Eq. (3) and making use of the Fermionic commutation relations, in this case we get:

$$\begin{aligned} H^c_{i_1 j_1 i_2 j_2, i_1' j_1' i_2' j_2'} = {} & (\epsilon_{i_1} + \epsilon_{i_2} + \epsilon_{j_1} + \epsilon_{j_2}) \delta_{i_1 j_1, i_1' j_1'} \delta_{i_2 j_2, i_2' j_2'} \\ & - (\epsilon_{i_1} + \epsilon_{i_2} + \epsilon_{j_1} + \epsilon_{j_2}) \delta_{i_1 j_1, i_1' j_2'} \delta_{i_1 j_2, i_2' j_1'} \\ & - (\epsilon_{i_1} + \epsilon_{i_2} + \epsilon_{j_1} + \epsilon_{j_2}) \delta_{i_1 j_1, i_2' j_1'} \delta_{i_2 j_2, i_1' j_2'} \\ & + (\epsilon_{i_1} + \epsilon_{i_2} + \epsilon_{j_1} + \epsilon_{j_2}) \delta_{i_1 j_1, i_2' j_2'} \delta_{i_2 j_2, i_1' j_1'}. \end{aligned} \tag{C10}$$

In a similar way, combining Eq. (C6) with the explicit form of the carrier-carrier Hamiltonian $\mathbf{H}^{cc}$ in Eq. (4), after a straightforward calculation we obtain

$H^{cc}_{i_1 j_1 i_2 j_2, i_1' j_1' i_2' j_2'}$

$$\begin{aligned} = {} & \frac{1}{2}(V_{i_1 i_2 i_1' i_2'} - V_{i_2 i_1 i_1' i_2'} - V_{i_1 i_2 i_2' i_1'} + V_{i_2 i_1 i_2' i_1'})(\delta_{j_1 j_2, j_1' j_2'} - \delta_{j_1 j_2, j_2' j_1'}) + \frac{1}{2}(V_{j_1 j_2 j_1' j_2'} - V_{j_2 j_1 j_1' j_2'} - V_{j_1 j_2 j_2' j_1'} \\ & + V_{j_2 j_1 j_2' j_1'})(\delta_{i_1 i_2, i_1' i_2'} - \delta_{i_1 i_2, i_2' i_1'}) - V_{i_1 j_1 i_1' j_1'} \delta_{i_2 j_2, i_2' j_2'} + V_{i_1 j_1 i_1' j_2'} \delta_{i_2 j_2, i_2' j_1'} + V_{i_1 j_2 i_1' j_1'} \delta_{i_2 j_1, i_2' j_2'} - V_{i_1 j_2 i_1' j_2'} \delta_{i_2 j_2, i_1' j_1'} \\ & + V_{i_1 j_1 i_2' j_1'} \delta_{i_2 j_2, i_1' j_2'} - V_{i_1 j_1 i_2' j_2'} \delta_{i_2 j_2, i_1' j_1'} - V_{i_1 j_2 i_2' j_1'} \delta_{i_2 j_1, i_1' j_2'} + V_{i_1 j_2 i_2' j_2'} \delta_{i_2 j_1, i_1' j_1'} + V_{i_2 j_1 i_1' j_1'} \delta_{i_1 j_2, i_2' j_2'} - V_{i_2 j_1 i_1' j_2'} \delta_{i_1 j_2, i_2' j_1'} \\ & - V_{i_2 j_2 i_1' j_1'} \delta_{i_1 j_1, i_2' j_2'} + V_{i_2 j_2 i_1' j_2'} \delta_{i_1 j_1, i_2' j_1'} - V_{i_2 j_1 i_2' j_1'} \delta_{i_1 j_2, i_1' j_2'} + V_{i_2 j_1 i_2' j_2'} \delta_{i_1 j_2, i_1' j_1'} + V_{i_2 j_2 i_2' j_1'} \delta_{i_1 j_1, i_1' j_2'} - V_{i_2 j_2 i_2' j_2'} \delta_{i_1 j_1, i_1' j_1'}. \end{aligned} \tag{C11}$$

Let us finally discuss the explicit form of the carrier-light matrix elements (19) entering the many-exciton absorption probability in Eq. (20).

For the excitonic absorption [see Eq. (22)] the corresponding matrix elements are defined in Eq. (23). Combining the explicit form of the carrier-light interaction Hamiltonian (14) with that of the generic excitonic state in Eq. (21), we get

$$H'_{\lambda_1 0} = -E(t) \sum_{l_1} U^{\lambda_1 *}_{l_1} \mu^*_{l_1}, \tag{C12}$$

where $U^{\lambda_1}_{l_1}$ is the unitary transformation from the noninteracting basis to the interacting one, l_1 is the noninteracting two-particle label corresponding to the single-particle states i_1 and the j_1, while $\mu_{l_1} \equiv \mu_{i_1 j_1}$ is the single-particle dipole matrix element given in Eq. (15).

For the biexcitonic absorption [see Eq. (26)] the corresponding matrix elements are defined in Eq. (27). Combining the explicit form of the carrier-light interaction Hamiltonian (14) with that of the excitonic state in Eq. (21) as well as of the biexcitonic state in Eq. (25), we obtain

$$H'_{\lambda_2 \lambda_2} = -E(t) \sum_{l_2} U^{\lambda_2 *}_{l_2} \{ (U^{\lambda_1}_{i_1 j_2} \mu^*_{i_2 j_1} + U^{\lambda_1}_{i_2 j_1} \mu^*_{i_1 j_2}) \times (2\delta_{i_1 i_2, j_1 j_2} - 1) - U^{\lambda_1}_{i_1 j_1} \mu^*_{i_2 j_2} - U^{\lambda_1}_{i_2 j_2} \mu^*_{i_1 j_1} \}, \tag{C13}$$

where again $U^{\lambda_N}_{l_N}$ is the unitary transformation from of the noninteracting N-particle basis to the interacting one, μ is the single-particle dipole matrix element, and $l_2 \equiv i_1 j_1, i_2 j_2$ is the generic label for the noninteracting two-pair basis.

[1] See, e.g., G. Bastard, *Wave Mechanics of Semiconductor Heterostructures*, Les Editions de Physique (Les Ulis, France, 1989); *Theory of Transport Properties of Semiconductor Nanostructures*, edited by E. Schöll (Chapman & Hall, London, 1998).

[2] See, e.g., F. Rossi, Semicond. Sci. Technol. **13**, 147 (1998).

[3] See, e.g., T. Kuhn, in *Theory of Transport Properties of Semiconductor Nanostructures*, edited by E. Schöll (Chapman & Hall, London, 1998), p. 173.

[4] See, e.g., L. Jacak, P. Hawrylak, and A. Wojs, *Quantum Dots* (Springer, Berlin, 1998); D. Bimberg *et al.*, *Quantum Dot Heterostructures* (Wiley, Chichester, 1998).

[5] See, e.g., M. Rontani, F. Rossi, F. Manghi, and E. Molinari, Appl. Phys. Lett. **72**, 957 (1998); Solid State Commun. **112**, 151 (1999); U. Hohenester, F. Rossi, and E. Molinari, *ibid.* **111**, 187 (1999); F. Troiani, U. Hohenester, and E. Molinari, Phys. Rev. B **62**, R2263 (2000); I. D'Amico and F. Rossi, Appl. Phys. Lett. **79**, 1676 (2001).

[6] See, e.g., R. Rinaldi *et al.*, Phys. Rev. B **62**, 1592 (2000).

[7] See, e.g., H. Saito *et al.*, Appl. Phys. Lett. **78**, 267 (2001); O. Shchekin *et al.*, *ibid.* **77**, 466 (2000).

[8] See, e.g., J. J. Finley *et al.*, Appl. Phys. Lett. **73**, 2618 (1998); G. Yusa and H. Sakaki, *ibid.* **70**, 345 (1997); T. Lundström *et al.*, Science **286**, 2312 (1999).

[9] See, e.g., M. Jr Bruchez *et al.*, Science **281**, 2013 (1998).

[10] See, e.g., D. Loss and D. P. DiVincenzo, Phys. Rev. A **57**, 120 (1998); M. Sherwin *et al.*, *ibid.* **60**, 3508 (1999); T. Tanamoto *ibid.* **61**, 022305 (2000).

[11] See, e.g., B. T. Miller *et al.*, Phys. Rev. B **56**, 6764 (1997); S. Tarucha *et al.*, Phys. Rev. Lett. **77**, 3613 (1996); E. Deckel *et al.*, *ibid.* **80**, 4991 (1998); L. Landin *et al.*, Science **280**, 262 (1998); F. Findeis *et al.*, Solid State Commun. **114**, 227 (2000).

[12] M. Bayer *et al.*, Phys. Rev. B **58**, 4740 (1998); U. Banin *et al.*, Nature (London) **400**, 542 (1999).

[13] P. Hawrylak *et al.*, Phys. Rev. Lett. **85**, 389 (2000); M. Bayer *et al.*, Nature (London) **405**, 923 (2000).

[14] P. Zanardi and F. Rossi, Phys. Rev. Lett. **81**, 4752 (1998).

[15] E. Biolatti, R. C. Iotti, P. Zanardi, and F. Rossi, Phys. Rev. Lett. **85**, 5647 (2000).

[16] Z. R. Wasileweski *et al.*, J. Cryst. Growth **201/202**, 1131 (1999); S. Fafard *et al.*, Phys. Rev. B **59**, 15 368 (1999); R. Leon *et al.*, *ibid.* **58**, R4262 (1998); J. M. Garcia *et al.*, Appl. Phys. Lett. **71**, 2014 (1997).

[17] P. Hawrylak, Phys. Rev. B **60**, 5597 (1999).

[18] See, e.g., P. Y. Yu and M. Cardona, *Fundamentals of Semiconductors* (Springer-Verlag, Berlin, 1996).

[19] See, e.g., G. Bastard, *Wave Mechanics of Semiconductor Heterostructures*, Les Editions de Physique (Les Ulis, France, 1989).

[20] Since the Hamiltonian in Eq. (1) is spin-independent, the single-particle wave function is given by the product of an orbital times a spin part $\psi_{i/j}(\mathbf{r}) = \phi_{e/h}(\mathbf{r}) \chi_{\sigma_{e/h}}$. Therefore, all the energy levels $\epsilon_{i/j}$ will be spin degenerate.

[21] See, e.g., W. Quade, E. Schöll, F. Rossi, and C. Jacoboni, Phys. Rev. B **50**, 7398 (1994).

[22] See, e.g., F. Rossi, R. Brunetti, and C. Jacoboni, in *Hot Carriers in Semiconductor Nanostructures: Physics and Applications*, edited by J. Shah (Academic, Boston, 1992) p. 153.

[23] See, e.g., P. Zanardi, Phys. Rev. A **57**, 3276 (1998), and references therein.

[24] F. Rossi and E. Molinari, Phys. Rev. Lett. **76**, 3642 (1996); Phys. Rev. B **53**, 16 462 (1996).

[25] F. Troiani, U. Hohenester, and E. Molinari, Phys. Rev. B **62**, R2263 (2000).

[26] N. H. Bonadeo *et al.*, Science **282**, 1473 (1998).

[27] L. Quiroga and N. F. Johnson, Phys. Rev. Lett. **83**, 2270 (1999).

[28] See, e.g., D. P. DiVincenzo and C. Bennet, Nature (London) **404**, 247 (2000), and references therein.

[29] J. I. Cirac and P. Zoller, Phys. Rev. Lett. **74**, 4091 (1995); T. Pellizzari *et al.*, *ibid.* **75**, 3788 (1995); C. Monroe *et al.*, *ibid.* **75**, 4714 (1995); A. Sorensen and K. Molmer *ibid.* **82**, 1971 (1999).

[30] Q. A. Turchette *et al.*, Phys. Rev. Lett. **75**, 4710 (1995); A. Imamoglu *et al.*, *ibid.* **83**, 4204 (1999).

[31] N. Gershenfeld and I. Chuang, Science **275**, 350 (1997).
[32] See, e.g., J. Shah, *Ultrafast Spectroscopy of Semiconductors and Semiconductors Nanostructures* (Springer, Berlin, 1996).
[33] A. Shnirman *et al.*, Phys. Rev. Lett. **79**, 2371 (1997); J. E. Mooij *et al.*, Science **285**, 1036 (1999).
[34] D. Loss and D. P. DiVincenzo, Phys. Rev. A **57**, 120 (1998); B. Kane, Nature (London) **393**, 133 (1998).
[35] M. Sherwin *et al.*, Phys. Rev. A **60**, 3508 (1999); T. Tanamoto, *ibid.* **61**, 022305 (2000).
[36] S. Lloyd, Science **261**, 1569 (1993).
[37] D. G. Cory *et al.*, quant-ph/0004104 (unpublished).
[38] Decoherence processes are accounted for in our density-matrix formalism by means of a standard T_1T_2 model: we employ a band-to-band recombination time $T_1=1$ ns and we describe phonon-induced decoherence processes in terms of an exciton-phonon dephasing time $T_2=50$ ps, which is compatible with the experimental values given in Ref. 26.
[39] Due to the short-range nature of the exciton-exciton dipole interaction [see Eq. (62)], we are allowed to consider nearest-neighbor coupling only. Indeed, for the specific quantum hardware considered (see Fig. 9), in view of the $1/D^3$ behavior and, more important, of their small oscillator strengths, second-neighbor couplings play no significant role.
[40] Q. A. Turchette *et al.*, Phys. Rev. A **61**, 063418 (2000).
[41] E. Pazy, I. D'Amico, P. Zanardi, and F. Rossi, Phys. Rev. B **64**, 195320 (2001).
[42] S. C. Benjamin, Phys. Rev. A **61**, 020301 (2000).
[43] The static dielectric constant ε_0 accounts for screening due to the crystal lattice only, i.e., due to the few-particle character of our system, free-carrier contributions should not be considered.